TOTAL MAGNETIC RECONNECTION DURING A TOKAMAK MAJOR DISRUPTION

by

JOHN ANTHONY GOETZ

A thesis submitted in partial fulfillment of the requirements for the degree of

Doctor of Philosophy
(Physics)

at the
UNIVERSITY OF WISCONSIN – MADISON
1990

TOTAL MAGNETIC RECONNECTION DURING A TOKAMAK MAJOR DISRUPTION

John Anthony Goetz
Under the supervision of Professor Stewart C. Prager

Magnetic reconnection has long been considered to be the cause of sawtooth oscillations and major disruptions in tokamak experiments. Experimental confirmation of reconnection models has been hampered by the difficulty of direct measurement of reconnection, which would involve tracing field lines for many transits around the tokamak. Perhaps the most stringent test of reconnection in a tokamak involves measurement of the safety factor q. Reconnection arising from a single helical disturbance with mode numbers m and n should raise q to m/n everywhere inside of the original resonant surface. Total reconnection should also flatten the temperature and current density profiles inside of this surface.

Disruptive instabilities (sawtooth oscillations and major disruptions) have been studied in the Tokapole II, a poloidal divertor tokamak. When Tokapole II is operated in the material limiter configuration (plasma boundary defined by the limiter plates), a major disruption results in current termination as in most tokamaks. However, when operated in the magnetic limiter configuration (plasma boundary defined by the magnetic separatrix) current termination is suppressed and major disruptions appear as giant sawtooth oscillations.

This objective of this thesis is to determine if total reconnection is occurring during major disruptions. To accomplish this goal, the poloidal magnetic field has been directly measured in Tokapole II with internal magnetic coils. A full two-dimensional measurement over the central current channel has been done. This is necessary due to the non-circularity of Tokapole II discharges. From these measurements, the poloidal magnetic flux function is obtained and the magnetic surfaces are plotted. The flux-surface-averaged safety factor, $q(\Psi)$, is obtained by integrating the local magnetic field line pitch over the experimentally obtained magnetic surface.

During a major disruption, the central safety factor jumps from below one to above one, while the total current is unchanged. Also, the toroidal current density profile is flattened during the disruption. This implies that total reconnection has occurred. This is in contrast to the absence of total reconnection previously observed [q(0) remained fixed at 0.7] during sawtooth oscillations in Tokapole II.

Acknowledgements

I would like to thank my advisor, Professor Stewart Prager, for his support and guidance during the course of this research and the years spent searching for a suitable thesis project. I would also like to thank Professor Richard Dexter for his help in construction of the magnetic probes that allowed me to perform the experiments for this thesis.

My colleagues Mike LaPointe, Ing Tan, and Ed Haines receive many thanks for helping to maintain Tokapole II and keep it running from day to day. Many thanks also go to the technical staff and all the other graduate students who have made my days here bearable.

To the Chicos: first there was Key lime pie in Hollywood, then the vegetable girl and Pee-Wee, what is there to do in Cincinnati? As far as spending all those hours trying to determine the effects of sidespin on a spherical projectile, need anything be said? To all those who spent hours on the Terrace discussing whatever, I will fondly remember those times.

Finally, I wish to acknowledge the love and support of my family. My parents never pushed or pulled me into this, they have just been at my side. My siblings have kept me going through these years in many ways. And to Cheryl, my fiancée, thank you for the love and support throughout these last few months and I hope to have sixty-nine years to explain to you just what it is I do for a living.

This work has been supported by the United States Department of Energy.

Table of Contents

Abstract ii
Acknowledgements iv
Table of Contents v

I. Introduction 1
I.A. Background 1
I.B. Overview of Thesis Research 3
I.B.1. Motivation for Thesis Research 3
I.B.2. Objective of Thesis Research and Research Approach 7
I.C. Organization of This Thesis 9
I.D. A Note About PLP and Thesis References 10
References 11

II. Status of Disruption Research 13
II.A. The Tokamak 13
II.A.1. Basic Concepts 13
II.A.2. Tokamak Instabilities 17
II.A.3. The Effects of Instabilities on Tokamak Operation 20
II.B. Sawtooth Oscillations 21
II.B.1. Experimental Observations of Sawteeth 22
II.B.1.a. Normal Sawteeth 22
II.B.1.b. Current Profile Measurements 24
II.B.1.c. Effects of Current Profile Modification 28
II.B.1.d. Sawteeth in the Large Tokamaks 29
II.B.2. Theoretical Investigations of Sawteeth 30
II.B.2.a. Mixing Models of Sawteeth 30
II.B.2.b. Turbulent Models of Sawteeth 33
II.B.3. Summary of Sawtooth Oscillations 34
II.C. The Disruptive Instability 35
II.C.1. Experimental Observations of Disruptions 36
II.C.1.a. Precursor Phase of Disruptions 37
II.C.1.b. Transport Phase of Disruptions 38
II.C.1.c. Termination Phase of Disruptions 39

II.C.1.d. Current and Density Limit Disruptions 40
II.C.2. Theoretical Investigations of Disruptions 40
II.C.2.a. (m,n) = (2,1) Tearing Mode Investigations 40
II.C.2.b. Multiple Helicity Tearing Mode Interactions 42
II.C.2.c. Coupled Tearing Mode–Transport Investigations 43
II.C.3. Disruption Control 44
II.C.4. Summary of Disruptions 47
References 48

III. Experimental Apparatus and Diagnostics 58
III.A. Tokapole II 59
III.B. General Diagnostics 65
III.C. Magnetic Probes and Analog Integrators 69
References 74

IV. Plasma Characteristics and Experimental Method 76
IV.A. Plasma Characteristics 76
IV.A.1. Global Characteristics of Plasmas with $q_a = 3$ 77
IV.A.2. Major Disruptions in Tokapole II 82
IV.B. Experimental Method (measurement of Ψ_p and $q(\Psi_p)$) 87
References 99

V. Experimental Results and Discussion 101
V.A. Experimental Results for Plasmas with $q_a = 3$ 101
V.A.1. Poloidal Magnetic Field Measurements 103
V.A.2. Poloidal Magnetic Surfaces 106
V.A.3. Flux-surface-averaged Safety Factor Profiles 108
V.A.4. Toroidal Current Density Profiles 113
V.B. Summary of Experiments 115
V.C. Suggestions for Future Work 117
References 121

Chapter 1

Introduction

I.A. Background

The primary goal in fusion energy research is to contain a high temperature plasma (usually a mixture of lighter elements such as deuterium and tritium) long enough that the energy released by the fusion reactions exceeds the energy used to contain and heat the plasma. In magnetic fusion the containment is provided by magnetic fields by exploiting the fact that the motion of charged particles perpendicular to the magnetic field is constrained. The tokamak is one of the leading concepts for attaining controlled nuclear fusion.

The subject of magnetohydrodynamic (MHD) stability has been studied for many years with the motivation for the research coming from astrophysics, space physics, controlled fusion research, geomagnetism, and many other fields. Some of the MHD instabilities that have been identified in controlled fusion research are believed to be due to magnetic reconnection processes. This thesis research will concentrate on investigating the reconnection process during a tokamak instability.

Tokamaks are designed to be stable in their normal operating regimes against the robust ideal MHD instabilities. However, a small but finite resistivity added to the ideal plasma (infinite conductivity) gives rise

to instabilities known as the resistive MHD instabilities.[1] These instabilities grow on a hybrid of the rapid Alfvén transit and slow resistive diffusion time scales and affect the evolution of the magnetic field structure and confinement of the plasma.[2] Finite resistivity allows the field lines to break and reconnect to form islands in the magnetic topology. These islands occur near the singular layers where helical perturbations to the equilibrium resonate with the pitch of the local magnetic field lines.

Tearing modes (resistive kink modes) are believed to be in some part responsible for three types of macroscopic MHD phenomena observed in tokamaks: Mirnov oscillations,[3] sawtooth oscillations,[4] and major disruptions.[5] Mirnov oscillations are fluctuations in the poloidal magnetic field that are detected at the edge of the plasma. The plasma confinement time decreases as the amplitude of the Mirnov oscillations increases. These oscillations have been interpreted as nonlinearly saturated magnetic islands generated by tearing modes that are rotating at the electron diamagnetic drift frequency.[6,7]

Sawtooth oscillations are repetitive relaxations in the soft x-ray emissivity and electron temperature of the plasma core. Sawteeth consist of a slowly rising phase during which the core is Ohmically heated and a rapid drop phase during which the plasma thermal energy is redistributed from the core to the periphery. This process limits the extent to which profiles can be peaked for optimal performance of the tokamak. Sawteeth may be useful as a means to remove accumulated impurities from the plasma core because they mix the core plasma with the edge plasma.

Major disruptions manifest themselves as a rapid broadening of the current and temperature profiles and often result in termination of the discharge. Tokamaks disrupt when the density or current exceeds a certain limit and thus disruptions limit the available operational regime. From an engineering viewpoint, disruptions cause significant erosion of surfaces and the rapid quench of the plasma current can cause significant mechanical stresses on the support structure of a reactor-grade vessel.

I.B. Overview of Thesis Research

I.B.1. Motivation for Thesis Research

The motivation for this thesis research is rooted in both experimental observations and theoretical investigations. This research builds upon work performed by many others, principally Drs. T.H. Osborne,[8] N.S. Brickhouse,[9] E. Uchimoto,[10] and R.A. Moyer.[11] These authors have investigated many novel features of disruptive instabilities in the Tokapole II poloidal divertor tokamak and have performed numerical simulations to investigate them. A summary of these features is shown in Figure 1.1 for magnetic limiter (plasma boundary defined by the magnetic separatrix) and material limiter (plasma boundary defined by limiter plates) discharges.

Tokamak discharges in Tokapole II have been obtained with the safety factor less than one over most of the plasma column. The safety

Features of Disruptive Behavior in Tokapole II

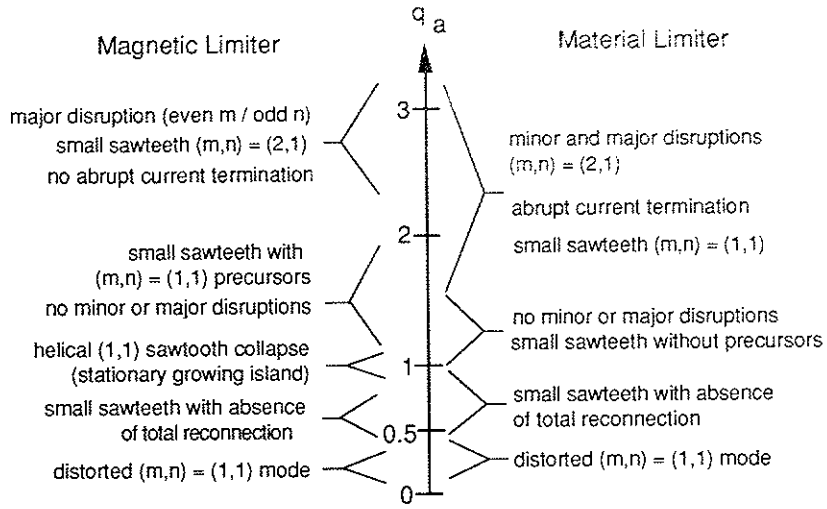

Figure 1.1
Key features of disruptive behavior in Tokapole II magnetic limiter (plasma boundary defined by the magnetic separatrix) and material limiter (plasma boundary defined by the material limiters) discharges over the range of operating parameters (from Reference 11).

factor, q, is the number of toroidal transits a field line makes in one poloidal transit of the torus. These discharges have normal sawtooth oscillations seen on soft x-ray detectors. A two-dimensional internal probe measurement of the poloidal magnetic field showed that $q(0) \cong 0.7$ and remained stationary through many sawtooth oscillations.[12,13] This

observation is in contradiction with the Kadomtsev model[14] that explains the sawtooth as a magnetic reconnection event.

In the Kadomtsev model of sawtooth dynamics, the collapse is attributed to a fast and complete reconnection of the helical flux inside and outside of the q = 1 surface. The reconnection is driven by the (m,n) = (1,1) tearing mode and should result in flattened current and temperature profiles inside of the q = 1 surface. The sawtooth cycle follows this mechanism: (1) q(0) falls below one and an m = 1 instability occurs, (2) a magnetic island forms and grows until the island center replaces the original magnetic axis, (3) q(0) should rise to unity (or above) after a sawtooth crash, and (4) the current density on axis increases until q(0) falls below one and the cycle begins again. A schematic showing the radial variation of the safety factor and the temporal evolution of the central safety factor is shown in Figure 1.2 for the Kadomtsev model.

The absence of complete reconnection during sawtooth oscillations in Tokapole II was at first attributed to the proximity of the q = 1 surface to the separatrix and the surrounding scrapeoff plasma. Measurements of the central q were then performed in sawtoothing discharges with the scrapeoff plasma removed (material limiter discharges).[15] Again, it was found that the central q was stationary and approximately 0.7 throughout many sawtooth oscillations.

A three-dimensional nonlinear resistive MHD computer code was developed by Uchimoto to investigate the effect of the divertor separatrix

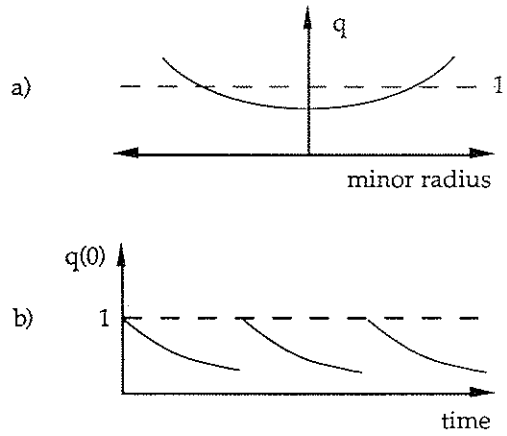

Figure 1.2
Schematic representation of the Kadomtsev[14] model of sawtooth dynamics showing a) the safety factor profile before a sawtooth and b) the temporal evolution of the central safety factor during sawteeth.

and the scrapeoff plasma on the evolution of the m = 1 resistive kink mode.[10] The code was specially constructed for the Tokapole II geometry including the separatrix and the scrapeoff plasma. Results from the computer runs indicated that total reconnection, with q(0) rising to unity, should occur in both magnetic and material limiter plasmas, i.e., with and without scrapeoff plasma.[16,17] Thus, the deviation of the experimental results from the Kadomtsev model does not appear within a resistive MHD description to be attributable to special features of the Tokapole II magnetic geometry.

Recent measurements of the magnetic field have been performed in

many tokamaks (see Section II.B.1.b.) in order to discern the behavior of q(0) during sawtooth oscillations. Many different diagnostic techniques have been used to make these measurements. The results obtained fall into two categories: (1) q(0) well below unity during sawtooth oscillations, and (2) q(0) near one with a flat central profile. In some tokamaks conflicting measurements of q(0) are obtained with different diagnostics in similar discharges. All of these measurements considered together may indicate that the sawtooth mechanism is not identical in every tokamak.

In magnetic limiter tokamak discharges with $q(a) \geq 2$ in Tokapole II, major disruptions, which appear as giant sawtooth oscillations, are obtained with a high degree of reproducibility.[18] These disruptions, although repetitive, are easily distinguished from the smaller sawtooth oscillations associated with the $q = 1$ surface.[8,9,11] The thermal loss of the plasma does not terminate the discharge since no material limiters are present for the plasma to contact during the minor radius expansion and inward major radius shift of the plasma during the disruption. When operated with limiter plates, the plasma terminates upon disruption as in most tokamaks.[11] The survival of the plasma presents the opportunity to track the magnetic behavior of the plasma through a major disruption.

I.B.2. Objective of Thesis Research and Research Approach

The objective of this thesis is to determine whether or not total

magnetic reconnection is occurring during major disruptions in Tokapole II. Experimental confirmation of total reconnection is difficult to achieve, although a stringent test of reconnection in a tokamak involves measurement of the safety factor. The safety factor should rise to m/n everywhere inside of the original m/n resonant surface if total reconnection arising from a single helical disturbance, with mode numbers m and n, is taking place during major disruptions. Also, the temperature and current density profiles should be flattened as a result of the reconnection. Tokapole II is operated in the magnetic limiter configuration so as to have repetitive major disruptions with pre-disruption, post-disruption and reheat phases to investigate.

The safety factor is obtained from a direct measurement of the poloidal magnetic field in a poloidal plane with internal magnetic coils and analog integration. From these measurements the poloidal magnetic flux function is obtained. The safety factor is then calculated on a flux surface and then averaged over that surface. The toroidal current density profile is also obtained from these magnetic measurements. The data will obtained from many discharges so that the analysis will take place at a fixed time that is phase referenced to a major disruption.

Previous measurements of the current density and safety factor profiles during major disruptions have been done in the LT-3 tokamak.[19] These experiments have shown that the current density profile is flattened in the center and that the edge current increases slightly during a major disruption. This corresponds to a rapid increase in the central safety factor.

The proposed experiment is unique in that (1) the magnetic surfaces and the safety factor are determined from a complete two-dimensional map of the poloidal magnetic field, (2) the post-disruption and reheat phases may be diagnosed since the plasma survives the disruption, and (3) the results of the measurements may be compared to the absence of total reconnection observed during sawtooth oscillations in the same device.

I.C. Organization of This Thesis

This thesis has been organized into five chapters. Chapter 2 contains an introduction to the tokamak confinement concept and tokamak instabilities. It also has a summary of the experimental and theoretical understandings of sawteeth and disruptions. This chapter may be omitted by readers familiar with disruption research. The Tokapole II device, its diagnostics, and the diagnostics unique to this research are discussed in Chapter 3. The experimental method followed and the characteristics of the plasmas investigated are presented in Chapter 4. Characteristics of major disruptions in Tokapole II are presented in this chapter. Chapter 5 contains the data obtained during this investigation. This includes safety factor and current density profiles. A summary and discussion of the results along with suggestions for future work are contained in this chapter.

I.D. A Note About PLP and Thesis References

Throughout this thesis, references are made to Ph.D. theses from the University of Wisconsin – Madison and PLP reports (which are internal reports of the University of Wisconsin Plasma Physics Group). Copies of these and detailed drawings of circuits and apparatus discussed in this thesis are available upon request from:

Plasma Physics Group, Department of Physics
University of Wisconsin – Madison
1150 University Avenue
Madison, WI 53706

REFERENCES

[1]H.P. Furth, J. Killeen, and M.N. Rosenbluth, Physics of Fluids, **6**, 459 (1963).

[2]J.D. Callen, B.V. Waddell, B. Carreras, M. Azumi, P.J. Catto, H.R. Hicks, J.A. Holmes, D.K. Lee, S.J. Lynch, J. Smith, M. Soler, K.T. Tsang, and J.C. Whitson, in *Plasma Physics and Controlled Nuclear Fusion Research 1978*, Proceedings of the 7th International Conference, Innsbruck (IAEA, Vienna, 1979), Vol. 1, p. 415.

[3]S.V. Mirnov and I.B. Semenov, Soviet Journal of Atomic Energy, **30**, 22 (1971).

[4]V.A. Vershkov and S.V. Mirnov, Nuclear Fusion, **14**, 383 (1974).

[5]E.P. Gorbunov and K.A. Razumova, Journal of Nuclear Energy, Part C: Plasma Physics, Accelerators, Thermonuclear Research, **6**, 515 (1964).

[6]R.B. White, D.A. Monticello, M.N. Rosenbluth, and B.V. Waddell, Physics of Fluids, **20**, 800 (1977).

[7]B. Carreras, B.V. Waddell, and H.R. Hicks, Nuclear Fusion, **19**, 1423 (1979).

[8]T.H. Osborne, Ph.D. thesis, University of Wisconsin (1984).

[9]N.S. Brickhouse, Ph.D. thesis, University of Wisconsin (1984).

[10]E. Uchimoto, Ph.D. thesis, University of Wisconsin (1988).

[11]R.A. Moyer, Ph.D. thesis, University of Wisconsin (1988).

[12]T.H. Osborne, R.N. Dexter, and S.C. Prager, Physical Review Letters, **49**, 734 (1982).

[13]T.H. Osborne, R.N. Dexter, and S.C. Prager, Physics of Fluids, **26**, 350, (1983).

[14]B.B. Kadomtsev, Soviet Journal of Plasma Physics, **1**, 389 (1975).

[15]R.A. Moyer, J.A. Goetz, R.N. Dexter, and S.C. Prager, Physics of Fluids B, **1**, 2139 (1989).

[16]S.C. Prager, Z. Chang, J.D. Callen, and E. Uchimoto, Bulletin of the American Physical Society, **33**, 1932 (1988).

[17]Y.Z. Agim, J.D. Callen, Z. Chang, R.N. Dexter, J.A. Goetz, D.E. Graessle, E. Haines, D. Kortbawi, M.A. LaPointe, R.A. Moyer, Z. Ning, S.C. Prager, T.D. Rempel, J.C. Sprott, I. Tan, and E. Uchimoto, in *Plasma Physics and Controlled Nuclear Fusion Research 1988*, Proceedings of the 12th International Conference, Nice (IAEA, Vienna, 1989), Vol. 1, p. 409.

[18]N.S. Brickhouse, J.D. Callen, R.N. Dexter, D.E. Graessle, D. Kortbawi, R.A. Moyer, T.H. Osborne, S.C. Prager, J.S. Sarff, J.C. Sprott, E. Uchimoto, C.K. Chu, J. DeLucia, A. Deniz, R.A. Gross, A.A. Grossman, A. Holland, F.M. Levington, M. Machida, T.C. Marshall, and G.A. Navratil, in *Plasma Physics and Controlled Nuclear Fusion Research 1984*, Proceedings of the 10th International Conference, London, (IAEA, Vienna, 1985), Vol. 1, p. 385.

[19]I.H. Hutchinson, Physical Review Letters, **37**, 338 (1976).

Chapter 2

Status of Disruption Research

The study of plasma properties in the tokamak configuration is an important part of controlled nuclear fusion research throughout the world. Both experimental and theoretical work have been progressing for years on this topic. As a result of this work, there have been advances made in the general understanding of magnetic reconnection processes. This chapter will provide a brief introduction to the tokamak confinement concept and tokamak instabilities along with a review of the body of knowledge concerning sawteeth and disruptions in tokamaks.

II.A. The Tokamak

II.A.1. Basic Concepts

One of the first devices used to attempt to achieve controlled nuclear fusion was the linear z-pinch.[1] In this device, a large current is driven parallel to the axis of a cylindrical plasma column. This current Ohmically heats the plasma and generates a poloidal magnetic field which compresses the plasma column and thus isolates it from the device walls. Instabilities that kink or pinch off the current channel are the bane of this simple type of discharge. These instabilities develop on the fast Alfvénic or ideal magnetohydrodynamic (MHD) time scale, $\tau_A = L\rho^{1/2}/B$, where L is

a characteristic length, ρ is the mass density, and B is the magnetic field of the plasma.

A close-fitting conducting shell and a strong magnetic field parallel to the plasma current can suppress these instabilities. The pinching instability is stabilized by the magnetic pressure of the additional field and the kink instability is suppressed by the shell and the magnetic tension of the field. The dire consequences of this additional field parallel to the plasma column is that the particles can easily flow along the field and escape the confinement device. A solution to this free-streaming problem is to connect the ends of the column by bending the cylinder into a torus and drive the plasma current inductively as the secondary of a transformer. This type of confinement device is known as the tokamak configuration.[2,3,4,5]

The magnetic field in a tokamak has three components: a toroidal field, a poloidal field, and a vertical field. The toroidal field is produced by coils wound around the plasma and provides for plasma stability as discussed previously. The poloidal field is produced by a current induced in the toroidal direction in the plasma by the transformer action of coils mounted coaxially with the torus. The poloidal field counteracts the vertical drift of particles (due to the non-uniformity of the toroidal field over the torus cross section) and prohibits vertical charge separation, thus providing plasma confinement. The vertical field is produced by another set of coaxial coils and interacts with the plasma current to balance the outward expansion force of the plasma and the plasma current.

The ratio of stabilizing toroidal magnetic field B_ϕ to the toroidal

plasma current I_p is an important parameter in tokamak stability. This ratio expressed in dimensionless form is known as the tokamak safety factor q, defined by:

$$q = \frac{2\pi}{\iota} \tag{2.1}$$

where ι is the rotational transform of the total magnetic field B. In a circular cross section tokamak, the safety factor can be expressed as:

$$q = \frac{d\phi}{d\theta} = \frac{r\, B_\phi}{R\, B_\theta} \tag{2.2}$$

where ϕ is the toroidal angle coordinate, θ is the poloidal angle coordinate, r is the minor radius, R is the major radius, and B_θ is the poloidal magnetic field. This coordinate system is depicted in Figure 2.1. In axisymmetric toroidal geometry,

$$q = \frac{d\Psi_{tor}}{d\Psi_{pol}} \tag{2.3}$$

where Ψ_{tor} is the toroidal magnetic flux within a magnetic surface and Ψ_{pol} is the poloidal magnetic flux between the center of the surface and the axis of the machine. In any type of toroidal geometry,

$$q = \lim \frac{\text{toroidal transits of a magnetic field line}}{\text{poloidal transits of a magnetic field line}} \tag{2.4}$$

where the limit is taken to an infinite number of toroidal transits of a magnetic field line.

Another parameter of importance in tokamak geometry is the plasma beta. The plasma beta is the ratio of the plasma energy density to the magnetic field energy density,

$$\langle\beta\rangle = \frac{\int p\, dV}{\int B^2/2\mu_0\, dV} \tag{2.5}$$

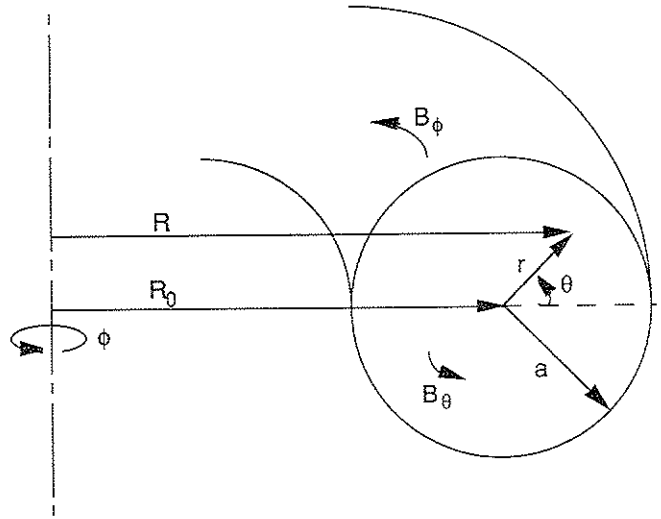

Figure 2.1
Toroidal geometry with the tokamak coordinate system: R (major radius), r (minor radius), ϕ (toroidal angle), and θ (poloidal angle). The major and minor radii of the torus are denoted by R_0 and a respectively.

where $p = \Sigma(nkT)$ is the plasma pressure and the integral is performed over the plasma volume. The "poloidal beta" is defined as

$$\beta_\theta = \frac{2\mu_0\langle p\rangle}{\langle B_\theta^2\rangle_{edge}} \tag{2.6}$$

where <p> is the volume averaged plasma pressure. For $\beta_\theta << 1$, the plasma is paramagnetic (causes an increase in B_ϕ) and the confinement is principally accomplished by the poloidal magnetic field. For $\beta_\theta >> 1$ the plasma is diamagnetic (causes a decrease in B_ϕ) and the confinement is done by the toroidal field. Typical values of β_θ are approximately equal to

one and this means that the confinement is accomplished equally by both magnetic fields and that the toroidal field is not affected much by the presence of plasma current.

II.A.2 Tokamak Instabilities

A plasma can be defined as a quasi-neutral gas of charged and neutral particles which exhibits collective behavior.[6] Even though a tokamak plasma is a many-bodied system, it can often be treated as a conducting fluid. The behavior of this fluid and the confining magnetic fields may be described by a magnetohydrodynamic (MHD) model. The tokamak equilibrium is obtained by balancing the outward force of the plasma and the poloidal magnetic field pressure with the vertical field. The stability of this equilibrium is investigated by studying the growth of small amplitude modes of the form $\xi_r = \xi(r) \exp[\, i(m\theta + n\phi + \omega t)]$, where ξ_r is a small radial perturbation to the equilibrium and m and n are the poloidal and toroidal mode numbers (integers) respectively. Modes for which the imaginary part of $\omega = \omega + i\gamma$ is negative are linearly unstable and will grow with growth rate γ. Another convenient way to determine the linear stability of a perfectly conducting plasma is to calculate the change in the potential energy δW when the system is perturbed. The system is unstable if δW is negative, that is the kinetic energy of the system has increased.

The radial positions of the singular magnetic surfaces, those

surfaces on which field lines close exactly after a small finite number of toroidal revolutions, are important in the MHD model. The safety factor on a singular surface has an integer value $q_s = m/n$. For these mode numbers the perturbation has the same pitch as the magnetic field lines and the bending of the magnetic field lines due to the perturbation, which is a stabilizing effect, is minimized.

The macroscopic MHD stability of a tokamak has been thoroughly studied in the infinite conductivity case (ideal MHD). Resistivity, even though it is small but finite, strongly influences the stability of various modes. In the MHD model, modes may be divided into three classes: axisymmetric modes, kink modes, and interchange modes. The current density gradient and the plasma pressure gradient are the main sources of free energy available to drive these instabilities.

Axisymmetric modes are only important in noncircular plasmas and can be controlled easily by careful shaping of the plasma and its boundary conditions. Interchange modes are driven by the pressure gradient and thus may limit the maximum attainable plasma pressure attainable in the tokamak configuration. Although these modes are important, this thesis research focuses on the effects of tearing modes, which are resistive kink modes.

Kink modes are driven by the current parallel to the magnetic field with their stability depending upon the current density profile.[7] In ideal MHD, a plasma can lower its magnetic energy by kinking into a helix with a pitch of (m,n). This can be envisioned as a rigid shift of the poloidal cross section in the direction of the displacement vector $\vec{\xi}$ which rotates

with a helical pitch of (m,n). The toroidal current density J_ϕ crosses the radial component of the perturbed magnetic field to give a poloidal force on the plasma. Because of the difference in current at different radii there is a net torque exerted on the plasma column. This torque drives the instability. A necessary condition for stability is that J_ϕ be not greater than zero at the plasma surface.[8]

The current density profile determines the location of the singular surfaces. The modes are associated with a singular surface but are not necessarily localized about the singular surface. In ideal MHD calculations with a vacuum region surrounding the plasma, these kink modes appear as perturbations to the plasma surface, and become very localized when the poloidal mode number m becomes large. For a circular tokamak with $R/r >> 1$, modes with resonant surfaces inside the plasma are stable, that is modes with $m/n < q(a)$ are stable.[8]

The assumption of perfect conductivity imposes the unreasonable constraint of fixed magnetic topology. Resistivity plays a critical role in a thin layer around the resonant surface $q = m/n$. It allows the tearing and reconnection of magnetic field lines to occur. When resistivity is included in MHD calculations, the plasma-vacuum boundary is no longer sharp and the modes are now found inside the plasma. Resistive kink modes are also known as tearing modes[9] and can dominate the low β MHD activity of the plasma. For very small values of resistivity, the tearing modes become unimportant.

The force driving the tearing mode instability is the same as the one driving the kink instability. The stability equation for the tearing mode

must be solved across a singularity at the resonant surface $q = m/n$. Tearing modes with $m > 3$ are stabilized by shear in the magnetic field. Low m-number tearing modes require the use of models of the current density and numerical solutions.

It is possible to stabilize the $m = 2$ and 3 modes by selecting the correct current profile although for normal profiles, these modes are unstable unless $q_0 > 2$ or 3 respectively. Proper shaping of the current density profile may be easily obtained in modern tokamaks. As in the ideal case, the $m = 1$ resistive mode must be considered separately. It is found that $q > 1$ everywhere is required for stability of this mode.[10] The condition $q(r) > 1$ imposes an upper limit on the current that can be driven through the plasma. This condition may be expressed as:

$$I_p\,(\mathrm{MA}) = \frac{r\,B_\theta}{2} < \frac{r^2\,B_\phi}{2\,R} \qquad (2.7)$$

An edge q value $q_a < 1$ is predicted to lead to a catastrophic instability.[7] This leads to the Kruskal–Shafranov condition:

$$I_p\,(\mathrm{MA}) < \frac{a^2\,B_\phi}{2\,R} \qquad (2.8).$$

II.A.3. The Effects of Instabilities on Tokamak Operation

A composite picture illustrating the various theoretical modes has been compiled.[8] It is seen that tokamak operation is generally in regions predicted to be unstable. The fact that tokamaks do operate satisfactorily indicates that there are conditions under which the nonlinear behavior of the instabilities is benign. As greater control has been exercised on the

plasma, the stable operating region has expanded considerably.[5]

The performance of a tokamak is influenced by a variety of instabilities. Microscopic instabilities may lead to anomalous transport and macroscopic instabilities lead to disruptions. A thorough understanding of the physics underlying these instabilities could lead to improved tokamak operation. Sawtooth oscillations limit plasma performance in the core of a tokamak discharge. A periodic degradation of the central confinement is a consequence of sawteeth. Thus sawteeth limit the maximum attainable central temperature and density. Disruptions set operational limits for the tokamak. It is well known that tokamaks disrupt when the density or the current exceeds a certain limit. Thus disruptions limit the available operational regime of tokamaks.

II.B. Sawtooth Oscillations

In 1973 at the Kurchatov Institute in the U.S.S.R. periodic relaxations in the soft x-ray emissivity were observed on the T-4 tokamak.[11] Similar observations were subsequently reported from the ST[12] and the ATC[13] tokamaks at the Princeton Plasma Physics Laboratory. These relaxation oscillations, known as sawtooth oscillations, have now been seen on all tokamaks and on many different diagnostics. The sawtooth phenomenon has been widely studied both experimentally and theoretically. Unfortunately, none of the theoretical models[14-23] is in complete agreement with all of the experimental data.

A review of both the experimental observations and the theoretical investigations of sawtooth oscillations will be presented here. The experimental observations can be divided into discussions of "normal sawteeth", current profile measurements during sawtooth oscillations, the influence of additional heating on the sawtooth, and sawteeth in large tokamaks with very low resistivity. The theoretical investigations can be divided into two categories depending on the mechanism causing the confinement degradation during a sawtooth collapse. These mechanisms are mixing of energy and particles due to either magnetic reconnection or the plasma flows associated with the (m,n) = (1,1) ideal kink mode and turbulence or stochasticity giving rise to enhanced diffusive radial transport.

II.B.1 Experimental Observations of Sawteeth

II.B.1.a Normal Sawteeth

The general characteristics of sawtooth oscillations are very similar in most tokamaks. A representation of a sawtooth cycle is shown in Figure 2.2 with the diagnostic shown being, for example, either SXR emissivity or electron temperature. The common characteristics of normal sawteeth include (1) a quiet phase during which the central temperature slowly rises, (2) a growing precursor oscillation, and (3) a rapid collapse of the central temperature coincident with a temperature rise in a ring around the central plasma. The central energy is redistributed during the collapse although no net energy is lost. The

inversion of the sawtooth collapse occurs at or near the q = 1 rational magnetic surface. The precursor oscillations have a (m,n) = (1,1) mode structure and are related to a magnetic island rotating around the q =1 surface. This island is caused by the growth of the (1,1) tearing mode with the evolution of this island being of importance to some theoretical models.

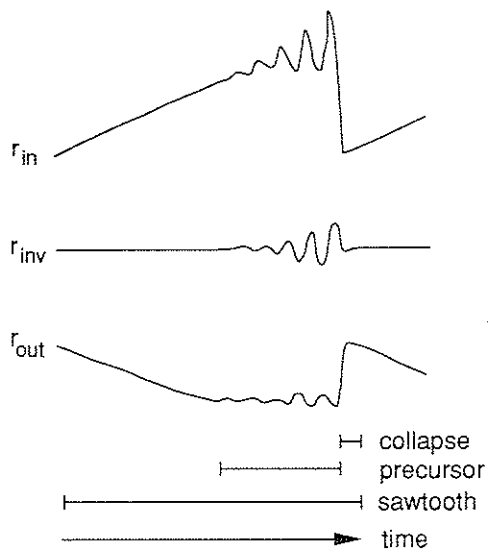

Figure 2.2
The time evolution of SXR emissivity or electron temperature during a normal sawtooth cycle at three different positions: inside (r_{in}), on (r_{inv}), and outside (r_{out}) the inversion radius which is where the sawtooth collapse changes sign.

Precursor oscillations in both the ORMAK[15] and TFR[24,25] tokamaks

have been studied. In ORMAK, the growth rate of the precursor oscillations is in agreement with the predicted linear growth rate of the (1,1) tearing mode. The sawtooth collapse was consistent with total reconnection[14] of the flux surfaces inside of the q = 1 surface to those outside of the q = 1 surface. In contrast, analysis of the TFR data showed that the sawtooth collapse could occur when the island was quite small and could not be described with a complete reconnection picture. The collapse was best described by a rapidly expanding zone of increased transport spreading through the plasma and originating at the island separatrix.

Supporting evidence for the existence of a mechanism for the collapse other than total reconnection is that the temperature profile after the sawtooth collapse in TFR and T-10[26] is not completely flat but remains somewhat peaked. Postcursor oscillations in TFR suggest that the magnetic island has survived the sawtooth collapse. Soft x-ray tomography in the PLT tokamak also indicates that the island has survived the collapse.[27]

II.B.1.b Current Profile Measurements

Information on the physics of sawteeth could be gained from accurate measurements of the current profile. Total reconnection of the (1,1) tearing mode to the magnetic axis should necessarily relax q(0) to one.[14,28] Measurements of the total magnetic field have been recently performed in many tokamaks. In various experiments, both q(0)

significantly below one and q(0) near one have been reported in discharges with sawtooth oscillations. There have also been conflicting measurements in similar discharges in the same tokamak.

Many experimental techniques have been developed in order to measure current density and safety factor profiles. These include Zeeman polarimetry using lithium beams, lithium pellets, and intrinsic impurities, Faraday rotation of FIR laser beams, driven resonant Alfvén waves, the imaging of H_α trails from ablating pellets, the Doppler shifted H_α emission from neutral hydrogen beams due to the motional Stark effect, laser induced fluorescence of an injected neutral beam, and direct magnetic probe measurements.

In the Tokapole II poloidal divertor tokamak, time resolved q profiles were obtained with a two-dimensional internal magnetic probe measurement showing q(0) = 0.7 and remaining stationary throughout many sawtooth cycles.[29,30] When the scrapeoff plasma beyond the divertor separatrix was removed, q(0) also remained stationary during sawtooth oscillations.[31] Boundary conditions have been removed as an explanation for q(0) remaining below one during sawteeth in this device.

In the TEXTOR tokamak, it was found by the Faraday rotation method that q(0) was well below one during a sawtooth cycle.[32] Since the current profile evolves on a long timescale compared to the sawtooth cycle, it was concluded that q remains well below one throughout sawtooth oscillations. Subsequent measurements in TEXTOR have shown that the relative change of the central current density is about 8%.[33]

This modulation indicates a rapid reconnection of the magnetic field lines although the Kadomtsev model is precluded by an average value of q(0) equal to 0.77.[33]

In the TEXT tokamak, measurements of the internal magnetic field structure are made by using laser-induced fluorescence of an injected neutral beam.[34] Using these measurements, the safety factor has been determined to be much less than one in discharges with sawteeth and above one in discharges without sawteeth. In the JET tokamak, the Faraday rotation method has been used to obtain the current density profile.[35] It was found that q(0) attains values of approximately 0.8 in both Ohmic and additionally heated plasmas. During stable periods, the central safety factor may be as low as 0.6. These measurements in JET are supported by calculations of the resistive diffusion of the current and by equilibrium analysis of external magnetic measurements.

In the PBX-M tokamak, the motional Stark effect has been exploited to polarize the emission from an injected neutral hydrogen beam.[36] The pitch angle of the magnetic field and thus the central safety factor can then be measured. It is found that q(0) = 0.86 in an Ohmic plasma and q(0) = 0.77 in a neutral beam heated plasma. These measurements are in agreement with previous measurements obtained with fast ion beams during startup on the same machine.[37]

In the Adiabatic Toroidal Compressor tokamak the orbit shifts associated with an injected fast ion beam have been used to measure the safety factor profile.[38] It was noticed that the sawtooth oscillation begins as soon as the q = 1 surface appears in the plasma and that q(0) remains very

near one as the edge safety factor is reduced. A neutral lithium beam probe has been used in the ASDEX tokamak to measure the magnetic pitch angle profile and thus obtain the safety factor profile.[39] The measured central q profile is flat, q(0) is just below one, and the location of the q = 1 surface corresponds to the sawtooth inversion radius as measured by electron cyclotron emission. In JET, the injection of deuterium pellets has been used to determine the location of mode rational surfaces.[40] The results of these experiments showed that q(0) is just less than one and that the q = 1 surface remains in the plasma for many sawtooth oscillations.

In the TEXT tokamak, the poloidal magnetic field profile has been measured using polarization spectroscopy of intrinsic[41] and injected impurities.[42] Both types of measurements show that q(0) averaged over many sawtooth periods in Ohmically heated sawtoothing discharges with varying q_a is very near unity. Alfvén waves have been used in the TCA tokamak to excite density oscillations that locate the resonance layer positions which depend on the value of the local safety factor.[43] It was found that the time-averaged (over many sawtooth periods) q profile had a flat central region with q(0) close to unity.

Much work and innovation has gone into developing novel ways to measure the current density profile in tokamaks. The results obtained fall into two categories: (1) q(0) well below unity during sawtooth oscillations, and (2) q(0) near one with a flat central profile. In some tokamaks both of these results are obtained depending on the diagnostic technique used. Further work must be done to make these measurements better time resolved and solve the discrepancies of these measurements.

II.B.1.c Effects of Current Profile Modification

Since the current profile plays an important role in sawtooth dynamics, any change in the profile should lead to sawtooth modification. The current profile may be changed directly by non-inductive current drive or indirectly by altering the temperature profile through additional heating. Electron cyclotron resonance heating (ECRH) is an appropriate method for auxiliary heating because its power deposition is well localized and easily controlled. ECRH experiments in T-10[26] with heating well outside the q = 1 surface led to broad temperature profiles without sawteeth. The results from TFR[44] showed that neither heating inside nor outside the q = 1 surface significantly affected the sawtooth behavior. Rather, heating on the q = 1 surface was shown to alter the sawtooth dynamics by significantly slowing the growth of the precursor and in some instances at high power levels saturated the mode.

Lower hybrid current drive (LHCD) has been the most successful method for non-inductive current drive experiments. A summary of experiments in ASDEX,[39] PETULA-B,[45] and PLT[46] indicates that sawteeth are stabilized if a sufficient amount of non-inductive current is driven, with this current being about 30-50% of the total current. In PETULA-B and ASDEX the current profile is observed to broaden with q(0) rising from just below one to just above one as the sawteeth disappear. Sawteeth are no longer present but a saturated (m,n) = (1,1) mode is seen in the PLT experiment. These facts indicate that there is no unique cause for sawtooth stabilization in non-inductive current drive experiments.

Stabilization occurs when q(0) rises above one, but is also possible when there is still a q = 1 surface present in the plasma.

II.B.1.d Sawteeth in the Large Tokamaks

In the large tokamaks (JET[47], TFTR[48], and JT-60[49]) the sawtooth behavior tends to be different than that of "normal" sawteeth. In these tokamaks, a more irregular and complex behavior of the central plasma is observed. Intermediate collapses occur at arbitrary times during the rise phase of the main sawtooth. These collapses do not alter the central plasma but redistribute energy in a ring around the sawtooth inversion radius. These large tokamak sawteeth also have the following characteristics: (1) no precursor to the main collapse is seen, although a postcursor oscillation sometimes occurs, (2) both pre- and postcursors are seen in connection with the intermediate collapse, (3) the duration of the collapse is very short, typically 50-200 μsec in JET,[47] which is as short as in much smaller tokamaks,[25,26] and (4) the main sawtooth collapse creates a completely flat or hollow temperature profile, with the profile remaining relatively flat if no auxiliary heating is applied.

Extensive studies of this sawtooth behavior have been performed in JET, including tomographic reconstruction of SXR measurements of the main sawtooth collapse.[50] These reconstructions indicate that the plasma core moves in a kink-like fashion with the kink being a (m,n) = (1,1) mode. Within 100 μsec the kink reaches a large amplitude, drawing a cold bubble into its wake, and within another 100 μsec the hot plasma and cold

bubble mix. This mixing is not complete and the poloidal asymmetry that results gives rise to the postcursor oscillation.

The intermediate collapse in JET has also been studied using the same methods.[51] The same kink-like movement of the plasma core is seen at the start of a collapse, but the kink never reaches a large amplitude, with the amplitude varying from one intermediate collapse to another. These facts suggest that the intermediate and main collapses have the same cause, but that the intermediate collapse is stopped at some point in its evolution. The collapse may be only intermediate because there is insufficient available free energy or because the final state is topologically inaccessible.

II.B.2 Theoretical Investigations of Sawteeth

II.B.2.a Mixing Models of Sawteeth

Essential to the mixing models is the explanation of the sawtooth collapse given by Kadomtsev.[14] He attributed the collapse to a fast and complete reconnection of the helical flux inside and outside of the q = 1 surface resulting in flattened current density and temperature profiles inside the q = 1 surface. The reconnection was assumed to be driven by the resistive kink or tearing mode. Numerical simulations[52,53,54] have confirmed the basic validity of the Kadomtsev model. However, the reconnection time predicted by this model is too long compared to the observed sawtooth collapse time in most tokamaks and the model predicts a single helicity (1,1) collapse, in contrast to the axisymmetric collapse seen

in most tokamaks.

A model based on growth of the m = 1 tearing mode has been formulated by Jahns et al.[15] with the following features: (1) during the collapse, the profiles are broadened and q is brought above one inside the resonant surface, (2) between disruptions the plasma relaxes back to an equlibrium described by a diffusive heat balance equation, and (3) q falls below one and the tearing mode begins to grow once again until a new collapse is induced. The second point makes this model distinct from the Kadomtsev model. In the center of the discharge, the relaxation is in the form of Ohmic heating and outside of the central region, the excess heat diffuses away. The predictions of this model agree well with the observations of sawtooth oscillations in ORMAK.[15] However, the peaked profiles seen in TFR[25] and T-10[26] after the collapse and the measurements of q(0) remaining less than one during the collapse in Tokapole II,[29-31] TEXTOR,[32,33] TEXT,[34] JET,[35] and PBX-M[36,37] are in clear contradiction with this model. These objections pertain to all models in which the mechanism for the collapse is complete reconnection. Furthermore, these models are unable to explain some of the features of the compound sawteeth seen in the larger tokamaks, neither the absence of a precursor on the main collapse nor the intermediate collapse that does not affect the core of the plasma.

Reconnection models with multiple q = 1 surfaces have been put forward to explain compound sawteeth.[16,17,55] Either complete or partial reconnection can take place leading to a main or an intermediate collapse,

respectively, depending on the details of the helical flux function. Since these models are founded on reconnection, the objections of the previous paragraph are again a concern.

An ideal MHD mechanism is suggested by the fast precursorless collapse of sawteeth in JET. Several authors have investigated the m = 1 stability of tokamaks in an attempt to explain the fast collapse.[18,56,57,58] These are the so called quasi-interchange models. When the shear inside the q = 1 surface is small, the growth rate of the kink mode is very sensitive to the minimum value of q. This may explain the short duration of the precursorless collapse and predicts a plasma flow during the collapse that is similar to that seen in JET.[50] Reconnection is incorporated into this model, but is assumed to occur only after the collapse has occurred and on a slow timescale. This model requires low shear in the plasma center and thus is inconsistent with all the data showing q(0) much less than one. Also, the plasma flows should flatten the profiles, thus leaving the observations of peaked profiles unaccounted for.

The modified Kadomtsev model is an attempt to describe all of the observed characteristics of normal sawteeth.[59] The model relies on the coupling of the temperature and current density profiles during the rise phase of the sawtooth to explain the variety of sawtooth dynamics observed. Skin currents can create nonmonotonic q profiles with q below one in a narrow band at the resonance surface and $q(0) \equiv 1$. These nonmonotonic q profiles can change the structure of (m,n) = (1,1) tearing mode from that suggested by Kadomtsev and thus affect the precursor

structure. Depending on the central confinement and the resulting temperature profile, this model provides a continuous transition between sawteeth that are described by the Kadomtsev model and those sawteeth that have very small precursors. Sawteeth in TFR,[24] for which the amplitudes of the precursor and successor oscillations are comparable may be representative of the transition from the small ST[12] tokamak in which the precursor amplitude was dominant to the large JET[47,50] tokamak in which there is no precursor.

Within the framework of all these models it is possible to stabilize sawteeth by keeping q(0) above one. Another means of stabilization is to prevent the growth of the (1,1) tearing mode, which according to theory is possible by means of current drive or heating within the magnetic island. Whether or not this explains the observations in PETULA-B[45] and PLT[46] can not be stated with certainty.

II.B.2.b Turbulent Models of Sawteeth

Explanations for the sawtooth collapse in terms of a catastrophic increase of the diffusive radial transport have been advanced.[19-22] This enhanced transport is due to either micro-turbulence generated when some instability threshold is exceeded[19,20] or to global stochastization of the magnetic field lines caused by overlap of secondary islands.[21,22] In either model, the turbulence is generated when the (1,1) island exceeds a critical size. Thus the models require a knowledge of the evolution of the

island and of the critical size of the island. In order to predict the final state after a collapse, information is needed about how large the radial transport is, how long the enhanced transport lasts, and what happens to the magnetic island and the current profile during the collapse.

These models can explain some of the experimental data that can not be explained by the mixing models. Because the collapse is due to diffusive transport, the profiles may remain peaked and the current profile need not change as dramatically as in the total reconnection case so that q(0) may remain well below one. The persistence of the magnetic island is not inconsistent with turbulent models. However, the complex behavior of sawteeth in the large tokamaks and the plasma flows in JET can not be explained with a turbulent mechanism.

Again sawteeth are stabilized when q(0) is raised above one or when a saturation of the island is achieved at an island size smaller than the critical island size. In the second case, stabilization of sawteeth by heating within the magnetic island or current drive may be possible because of the slower resistive growth of the mode (compared to the ideal mode).

II.B.3 Summary of Sawtooth Oscillations

There are differences in the experimental findings and the theoretical models for sawteeth in tokamaks. Part of the database may be explained by the mixing models, yet another part of the database is in contradiction with these models. This latter part of the database may be understood in terms of the turbulent models. These facts suggest that the

sawtoothing behavior of a plasma is determined by two different phenomena; mixing and turbulence. In cases that agree with the mixing models the profiles in the plasma core are relatively broad, whereas in cases that agree with the turbulent models the central profiles are peaked.

The database can be divided into a high shear regime with q(0) well below one and a low shear regime with q close to one in the plasma core. High shear is present in those cases for which the profiles remain peaked after a collapse. Most "normal" sawteeth belong in this regime and can be explained satisfactorily with a turbulent model. Low shear is present in those cases where the profiles are broad and become flattened or hollow during a collapse. These cases can be described with a mixing model. Large tokamaks are in the low shear regime since mixing models offer an explanation for fast collapses and compound sawteeth.

II.C. The Disruptive Instability

The major disruption is probably the most important phenomenon limiting the range of operation for tokamaks. Disruptions manifest themselves as violent MHD activity on a variety of timescales. A major disruption terminates the discharge after broadening the current profile whereas a minor disruption does not terminate the discharge. There is not only theoretical interest in understanding such dramatic MHD behavior but practical interest also. Since disruptions set operational limits, it is desirable to understand the mechanism of disruptions in order to improve tokamak operation and performance. From an engineering

viewpoint, disruptions can lead to significant erosion of surfaces and stresses on the support structure of a reactor-like vessel. Thus an understanding of disruptions should enhance the prospects of obtaining controlled nuclear fusion.

A review of both the experimental observations and the theoretical investigations of disruptions will be presented here. Also presented in this section will be a discussion of the methods used to control disruptions in fusion experiments. Disruptions generally fall into one of three classes: (1) loss of equilibrium, (2) current limit, and (3) density limit. The theoretical models used to describe the triggering of disruptions in tokamaks can be divided into three categories: (1) single helicity (m,n) = (2,1) tearing mode interaction with the limiter, (2) nonlinear interaction of tearing modes of different helicity, and (3) coupling of tearing modes with transport effects induced by island structures.

II.C.1. Experimental Observations of Disruptions

The external manifestations of disruptions are very similar in most tokamaks. These include (1) a large negative spike on the loop voltage of the plasma, (2) a sudden decrease in the major radius of the plasma, (3) a significant loss of particles and plasma energy from the core of the plasma, and (4) a decrease in the current ranging from a few percent to a termination of the discharge. For "minor" disruptions, the plasma current is only affected slightly and the discharge may survive many

minor disruptions. A "major" disruption terminates the discharge.

Although these manifestations may be similar in most tokamaks, the MHD behavior prior to and during a disruption and the final state of the plasma after a disruption vary in different machines. A disruption may be divided into precursor, transport, and termination phases in order to ease the discussion of experimental observations from many tokamaks.[60] The plasma thermal energy is lost during the transport phase to the limiters and the plasma magnetic energy is lost during the termination phase to the walls through radiation and charge exchange.

II.C.1.a Precursor Phase of Disruptions

A growing (m,n) = (2,1) magnetic oscillation during the precursor phase is a common feature of disruptions in most tokamaks.[11,51,61-70] However, sometimes disruptions are seen with a dominant (3,1) mode or with no precursor oscillations.[65,71,72] In some tokamaks, the (2,1) mode grows explosively just before the disruption. In other tokamaks the (2,1) mode grows to a saturated state while rotating in the electron diamagnetic drift direction. A typical feature in the precursor phase is the slowing down of the (2,1) mode as the mode grows and often the mode stops rotating completely.[61,63,70,73]

Once the (2,1) mode grows beyond a certain size, it may couple with other modes. In particular, a rapidly growing (3,2) mode[67,70] and a (5,3) mode[67] are seen just before the disruption. The (2,1) mode has also been seen to couple to the (1,1) mode in the interior of the discharge.[61-63,65,69]

In the JIPP T-II tokamak, coupling between the (2,1) and (3,2) modes and coupling between the (2,1) and (1,1) modes leads to different final states of the plasma.[74] Coupling between the (2,1) and (3,2) modes results in a minor disruption that redistributes the current between the $q = 3/2$ and $q = 2$ surfaces while leaving the core unaffected. Coupling between the (2,1) and (1,1) modes results in a major disruption that destroys confinement all the way to the center of the plasma. The TFR tokamak also reports that coupling of the (2,1) and the (1,1) modes leads to a major disruption.[63]

II.C.1.b Transport Phase of Disruptions

The transport phase of a disruption begins with the drop in the central electron temperature and the negative loop voltage spike. In PULSATOR,[61] a series of hard x-ray ($E \geq 1$ MeV) bursts, synchronized with the rotation of the helical mode, was observed to be emitted from the limiter. It was seen that the temperature drop in the center of the plasma occurred 10-30 μsec after the main burst of hard x-rays and 10-20 μsec before the leading edge of the negative loop voltage spike. These facts indicate that the central confinement was destroyed before the loop voltage spike occurred.

Internal magnetic probe measurements of the current show that at the time of the loop voltage spike, the central current falls rapidly and the edge current increases slightly.[75-78] This drop in current causes a drop in the plasma inductance ($l_i \sim B_\theta^2$), a drop in the poloidal β_θ ($\beta_\theta \sim T_e$), and expulsion of poloidal magnetic flux from the discharge. These changes are

the primary cause of the negative loop voltage spike. A rapid expansion in minor radius of the plasma column is also a contributing factor to the loop voltage spike. Such a rapid expansion is in agreement with the H_α emission and fast neutral particle efflux.

Due to the lowered plasma inductance and poloidal beta, the discharge shifts inward in major radius in an attempt to find a new equilibrium position. This movement is on a very fast, nearly ideal MHD timescale. The applied vertical field (Section II.A.1) can not respond on this fast timescale and thus can not stop the plasma from contacting the inner limiter and wall. This contact with the wall or limiter terminates the discharge through rapid cooling and the influx of impurities.[28,61,62,69,79] In some tokamaks, the discharge is not terminated by a disruption and achieves a new equilibrium position due to the fact that there is no plasma-wall interaction.[28,80]

II.C.1.c Termination Phase of Disruptions

The termination phase of a disruption is characterized by a nearly linear current rampdown rate. In some tokamaks the rampdown rate depends on the magnitude of the central temperature drop and/or the amount of plasma-limiter contact.[61,79] The rate has also been seen to depend on the strength of minor disruptions which affect the plasma edge.[62,69,74] In either case, it is seen that the current rampdown rate depends on the severity of the transport phase. The boundary conditions

of the plasma also affect the current rampdown rate.[81]

II.C.1.d Current and Density Limit Disruptions

Along with the loss of equilibrium as a cause of major disruption, there are current limit and density limit disruptions observed in tokamaks. Current limit and density limit disruptions restrict the operating regime of a tokamak to lie within a triangle of the Hugill diagram, which is a plot of the Murakami parameter[82] nR/B_ϕ versus $1/q_a$. The current limit is $q_a \geq 2$ and the density limit, which is proportional to the average current density, is $n < CB_\phi/Rq_a$, where C is a machine-dependent number usually between 1-2 x 10^{20} Wb^{-1} for Ohmically heated plasmas. There is some variation in how closely the $q_a = 2$ limit can be approached with $q_a \approx 2$ operation reported from some tokamaks[51,83,84] and $q_a \approx 2.2$ reported from others.[66,70] The density limit can be increased somewhat by neutral beam injection[85,86] (which increases the amount of heating) and pellet fueling[86] (which reduces the impurity fraction).

II.C.2 Theoretical Investigations of Disruptions

II.C.2.a (m,n) = (2,1) Tearing Mode Investigations

One of the earliest models used to describe major disruptions found that the nonlinear development of ideal kink modes in a cylindrical plasma with a flat (shearless) current profile traps pockets of vacuum or cold plasma in the plasma periphery. These bubbles are convected inward

by the plasma flows associated with the kinks.[87] The inclusion of shear to the model reduces the distortion of the plasma from the kinks which brings about the conclusion that ideal kink modes are not responsible for disruptions.[88]

As discussed in Section II.A.2, the ideal kink modes become tearing modes when resistivity is included. The growth of the (2,1) tearing mode can be halted by a self-stabilization through quasi-linear flattening of the current density profile which reduces the destabilizing current density gradient.[89] The saturated island width is determined by the equilibrium current density and resistivity profiles. For profiles with sufficiently high shear, the island will saturate at a width $w \leq 0.4a$.[90] This saturation of the magnetic island at a small size explains the persistence of (2,1) magnetic oscillations in the absence of disruptions. However, the $q = 2$ magnetic island can grow until it encompasses the entire plasma cross section when the magnetic shear is sufficiently weak ($1.5 \leq q(0) \leq 1.8$).[90,91] As the large islands grow, the high conductivity core plasma is convected outward and the low conductivity edge plasma moves to the center.[92] Thus central confinement is lost during the development of these large islands.

For profiles with low shear and low current density at the $q = 2$ mode rational surface, the (2,1) mode is further destabilized if the (2,1) island makes contact with a limiter or a cold gas region.[93] This contact cools the island and decreases the current density near the island O-point, which enhances the island growth. Since the magnetic island grows mainly inward due to profile effects,[89] q_a must be near two for the island

to come in contact with the limiter or the cold gas region. Thus, this scenario may offer an explanation for the observed $q_a \geq 2$ current limit.

II.C.2.b Multiple Helicity Tearing Mode Interactions

Three-dimensional MHD simulations[94-96] showed that when the (2,1) tearing mode creates a large island it can strongly destabilize the (3,2) mode and higher harmonics. The (2,1) tearing mode grows by feeding off the local current gradient near the $q = 2$ surface and thereby steepens the gradient at smaller radii. This steep current gradient destabilizes the (3,2), (5,3) and other harmonics, eventually leading to a turbulent spectrum of modes. The three-dimensional nonlinear interaction of these resistive modes is a mechanism that results in stochastic magnetic fields and the loss of confinement over a large region of the plasma. Although the work of References 94-96 has been questioned as to its numerical accuracy, several independent simulations have verified the destabilization of the (3,2) and higher order modes.[97-99]

While this mechanism of stochasticity is a plausible explanation of disruptions, not all features of major disruptions are consistent with this model. Although the (2,1) mode is almost universally seen, it is not clear that the (3,2) and higher order modes are as ubiquitous (see Section II.B.2.a). The turbulent fluctuations are localized in the periphery of the plasma and simulations in which the temperature is evolved self-consistently with the magnetic fluctuations, the central confinement is not significantly degraded.[96] Thus it is not clear why this turbulence should

necessarily disrupt the entire plasma. An additional difficulty with these multiple helicity models is the assumption of an initial equilibrium that is highly unstable to the (2,1) mode, without giving a physical reason for such an equilibrium to arise.

II.C.2.c Coupled Tearing Mode–Transport Investigations

To a great extent, the temperature and current profiles in the plasma are determined by microscopic transport processes. However, when large scale MHD phenomena occur (sawteeth, islands, etc.) the magnetic field structure is affected and the transport changes. Transport processes have been coupled to tearing mode calculations using one-dimensional transport models to evolve the temperature profile self-consistently in the presence of large magnetic islands.[100,101]

This self-consistent evolution included thermal conduction, Ohmic heating, and radiation losses. When an island developed, the temperature was flattened across the island. Sawteeth effects were modelled by a large increase in the thermal conductivity in the region where $q < 1$. The current profile is evolved according to a one-dimensional diffusion equation with Spitzer resistivity ($\eta \propto T^{-3/2}$). The interaction of different tearing modes does not include mode coupling but occurs through the quasi-linear modification of the current profile. Despite their simplicity, these models include the essential element of coupling transport processes and MHD instability.

The results of these simulations[100] suggest that disruptions involve

(1) a large magnetic island (most likely the (2,1) island) intersecting a limiter or cold gas region, (2) an intermediate island resonant between the $q = 2$ surface and the magnetic axis (ensuring connection across the entire minor radius), and (3) a method of restricting the amount of current flowing around the axis (either sawteeth or the accumulation of impurities near the axis).

When the simulations include transport and MHD phenomena within the framework of the three-dimensional reduced MHD equations, the following picture of major disruptions emerges:[98] (1) low current density at the $q = 2$ surface destabilizes the $(m,n) = (2,1)$ tearing mode which then destroys the confinement in the $q > 1$ region by nonlinear multiple helicity interactions, (2) the contraction of the central current channel causes $q(0)$ to fall below one after which an internal sawtooth-like instability strongly reduces the central temperature and $q(0)$ rises above one, and (3) the contracted current profile with $q(0) > 1$ is unstable to the toroidal $n = 1$ external kink which terminates the discharge. This model is in agreement with data from T-4,[62] JIPP-II,[74] and PLT.[65]

II.C.3 Disruption Control

Disruption control is centered on stabilization of the (2,1) tearing mode. The (2,1) mode is important because the $q = 2$ rational surface is located near the edge of the plasma in a region where the current density gradient is substantial (the current density gradient is destabilizing, see

Section II.A.2). The (2,1) mode is involved in loss of equilibrium, current limit, and density limit disruptions.

Attempts to increase the plasma density by gas puffing from the wall result in increased impurity input from the wall which cools the edge of the plasma. This cooling decreases the current density in the edge and thus increases the gradient near the q = 2 surface. The use of pellet injection to increase the plasma density avoids this effect and allows the disruptive density limit to be passed.[86] Improved wall cleanliness obtained through either pulsed cleaning or gettering decreases the impurity influx that results from wall recycling with heavy gas puffing. These methods have also resulted in increasing the disruptive density limit.[66,68,102,103]

It is observed experimentally that as the (2,1) mode begins to grow, the rotation frequency decreases and when the rotation stops, the disruption begins.[63,73] When the rotation frequency of the mode is much larger than the inverse time constant of the wall, the wall appears conducting and the mode may be stabilized. However, once the mode starts to grow, eddy currents induced in the resistive wall slow down the mode rotation which reduces the wall stabilization and the mode grows faster, etc.[104] As long as the q = 2 surface is inside the conducting plasma, the rotation frequency is determined by the plasma flow locally at the resonant surface. If the q = 2 surface moves to a region of low conductivity plasma, the (2,1) mode is free to rotate with respect to the rest of the plasma. Thus, the mode itself can lock to the wall and be thought of as an external kink, slowed down by the resistive wall. The current limit is

reached when the q = 2 surface approaches the edge of the plasma where the conductivity is sufficiently low for a wall locked mode to slip with respect to the plasma.[105] This condition agrees well with the experimentally observed limit $2.0 \leq q_a \leq 2.2$ where the range of values may be due to temperature profile differences.

The growth of the (2,1) island has been controlled with a resonant (m,n) = (2,1) winding. The applied field induced a small magnetic island that flattened the current density profile about the q = 2 surface.[61,102] Nonresonant windings have also been used to stabilize the (2,1) tearing mode. Windings with m/n > 2 have been used to stochasticize the magnetic fields causing transport that flattens the current density gradient near the q = 2 surface.[106] High shear is added to the magnetic field near the q = 2 surface by windings with m/n < 2 which stabilizes the mode.[107]

Since the current profile plays such an important role in the dynamics of the tearing mode, any change in the current profile should lead to modification of the tearing mode. In the TFR[108] tokamak ECRH has been used to suppress m = 2 and m = 3 activity in a discharge which exhibits strong MHD activity without the additional heating. The optimum position for heating was found to be approximately two centimeters outside of the q = 2 surface. Feedback stabilization has also been demonstrated in this experiment. A repeated suppression of the m = 2 activity was obtained with a feedback loop which switches on the ECRH when the m = 2 activity exceeded a preset level.

II.C.4 Summary of Disruptions

Major disruptions in tokamaks are characterized by an abrupt loss of energy confinement leading to a termination of the discharge. These disruptions are almost universally associated with growing (m,n) = (2,1) oscillations in both soft x-ray and magnetic signals. Progress has been made in obtaining a complete picture of the mechanism of a disruption. It is generally thought that the (m,n) = (2,1) tearing mode is in some manner responsible for triggering the disruption. This trigger may be contact of the resulting (2,1) island with the limiter or cold gas region, the nonlinear interaction of the (2,1) mode with tearing modes of different helicity, or the coupling of the (2,1) tearing mode with transport processes. There has also been gains made in trying to control disruptions and in trying to extend the current and density limits.

REFERENCES

[1]S.W. Cousins and A.A. Ware, Proceedings of the Physical Society, London, Section B, **64**, 159 (1951).

[2]A.D. Sakharov and I.E. Tamm, in *Plasma Physics and the Problem of Controlled Thermonuclear Reactions*, edited by M.A. Leontovich (Pergamon, New York, 1961), Vol. 1, p. 1-47.

[3]L.A. Artsimovich, Nuclear Fusion, **12**, 215 (1972).

[4]H.P. Furth, Nuclear Fusion, **15**, 487 (1975).

[5]J. Sheffield, Proceedings of the IEEE, **69**, 885 (1981).

[6]F.F. Chen, *Introduction to Plasma Physics* (Plenum Press, New York, 1984), p. 3.

[7]V.D. Shafranov, Soviet Physics – Technical Physics, **15**, 175 (1970).

[8]J.A.Wesson, Nuclear Fusion, **18**, 87 (1978).

[9]H.P. Furth, J. Killeen, and M.N. Rosenbluth, Physics of Fluids, **6**, 459 (1963).

[10]M.N. Bussac, D. Edery, R. Pellat, and J.L. Soule, in *Plasma Physics and Controlled Nuclear Fusion Research 1976*, Proceedings of the 6th International Conference, Berchtesgaden (IAEA, Vienna, 1977), Vol. 1, p. 607.

[11]V.A. Vershkov and S.V. Mirnov, Nuclear Fusion, **14**, 383 (1974).

[12]S. von Goeler, W. Stodiek, and N. Sauthoff, Physical Review Letters, 33, 1201 (1974).

[13]R.R. Smith, Nuclear Fusion, **16**, 1053 (1976).

[14]B.B. Kadomtsev, Soviet Journal of Plasma Physics, **1**, 389 (1975).

[15]G.L. Jahns, M. Soler, B.V. Waddell, J.D. Callen, and H.R. Hicks, Nuclear Fusion, **18**, 609 (1978).

[16]V.V. Parail and G.V. Pereverzev, Soviet Journal of Plasma Physics, 6, 14 (1980).

[17]W. Pfeiffer, Nuclear Fusion, **25**, 673 (1985).

[18]J.A. Wesson, Plasma Physics and Controlled Fusion, **28**, 243 (1986).

[19]A. Samain, Plasma Physics, **18**, 551 (1976).

[20]M.A. Dubois and A. Samain, Nuclear Fusion, **20**, 1101 (1980).

[21]C. Mercier, Soviet Journal of Plasma Physics, **9**, 82 (1983).

[22]A.J. Lichtenberg, Nuclear Fusion, **24**, 1277 (1984).

[23]A. Rogister, A. Kaleck, M. Psimopoulos, and G. Hasselberg, Physics of Fluids B, **2**, 953 (1990).

[24]M.A. Dubois, D. Marty, and A. Pochelon, Nuclear Fusion, **20**, 1355 (1980).

[25]M.A. Dubois, A.L. Pecquet, and C. Reverdin, Nuclear Fusion, **23**, 147 (1983).

[26]R.M.J. Sillen, H.W. Piekaar, T. Oyevaar, E. P. Gorbunov, A.A. Bagdasarov, and N.L. Vasin, Nuclear Fusion, **26**, 303 (1986).

[27]A. Compant La Fontaine, M.A. Dubois, and A.L. Pecquet, Plasma Physics and Controlled Fusion, **27**, 229 (1985).

[28]R.A. Moyer, Ph.D. thesis, University of Wisconsin (1988).

[29]T.H. Osborne, R.N. Dexter, and S.C. Prager, Physical Review Letters, **49**, 734 (1982).

[30]T.H. Osborne, R.N. Dexter, and S.C. Prager, Physics of Fluids, **26**, 350 (1983).

[31]R.A. Moyer, J.A. Goetz, R.N. Dexter, and S.C. Prager, Physics of Fluids B, **1**, 2139 (1989).

[32]H. Soltwisch, W. Stodiek, J. Manickam, and J. Schlüter, in *Plasma Physics and Controlled Nuclear Fusion Research 1986*, Proceedings of the 11th International Conference, Kyoto (IAEA, Vienna, 1987), Vol. 1, p. 263.

[33]H. Soltwisch, Review of Scientific Instruments, **59**, 1599 (1988).

[34]W.P. West, D.M. Thomas, J.S. deGrassie, and S.B. Zheng, Physical Review Letters, **58**, 2758 (1987).

[35]D.J. Campbell, J.G. Cordey, A.W. Edwards, R.D. Gill, E. Lazzaro, G. Magyar, A.L. McCarthy, J. O'Rourke, F. Pegoraro, F. Porcelli, P. Smeulders, D.F.H. Start, P. Stubberfield, J.A. Wesson, E. Westerhof, and D. Zasche, in *Plasma Physics and Controlled Nuclear Fusion Research 1988*, Proceedings of the 12th International Conference, Nice (IAEA, Vienna, 1989), Vol. 1, p. 377.

[36]F.M. Levinton, R.J. Fonck, G.M. Gammel, R. Kaita, H.W. Kugel, E.T. Powell, and D.W. Roberts, Physical Review Letters, **63**, 2060 (1989).

[37]D.D. Meyerhofer, R.J. Goldston, R. Kaita, A. Cavallo, B. Grek, D. Johnson, D.C. McCune, K. McGuire, and R.B. White, Nuclear Fusion, **25**, 321 (1985).

[38]R.J. Goldston, Physics of Fluids, **21**, 2346 (1978).

[39]K. McCormick, F.X. Söldner, D. Eckhartt, F. Leuterer, H. Murmann, H. Derfler, a. Eberhagen, O. Gehre, J. Gernhardt, G. v. Gierke, O. Gruber,

M. Keilhacker, O. Klüber, K. Lackner, D. Meisel, V. Mertens, H. Röhr, K.-H. Schmitter, K.-H. Steuer, and F. Wagner, Physical Review Letters, **58**, 491 (1987).

[40]A. Weller, A.D. Cheetham, A.W. Edwards, R.D. Gill, A. Gondhalekar, R.S. Granetz, J. Snipes, and J.A. Wesson, Physical Review Letters, **59**, 2303 (1987).

[41]D. Wróblewski, L.K. Huang, H.W. Moos, and P.E. Phillips, Physical Review Letters, **61**, 1724 (1988).

[42]L.K. Huang, M. Finkenthal, D. Wróblewski, H.W. Moos, W.P. West, D.M. Thomas, M.P. Thomas, X.Z. Yang, P.E. Phillips, A.J. Wooton, R.D. Bengston, J.A. Boedo, R.V. Bravenec, J.Y. Chen, G. Cima, K.W. Gentle, S.C. McCool, B.U. Richards, W.L. Rowan, D.C. Sing, and K.W. Wenzel, Physics of Fluids B, **2**, 809 (1990).

[43]H. Weisen, G. Borg, B. Joye, A.J. Knight, and J.B. Lister, Physical Review Letters, **62**, 434 (1989).

[44]TFR Group and FOM ECRH Team, in Proceedings of the Thirteenth European Conference on Controlled Fusion and Plasma Physics, Schliersee, FRG, 1986 (EPS, Geneva, 1986), Vol. II, p. 207.

[45]D. van Houtte, G. Briffod, P. Chabert, C. Gormezano, J. How, G. Ichtchenko, G. Melin, B. Monlin, F. Parlange, and J.C. Vallet, Nuclear Fusion, **24**, 1485 (1984).

[46]T.K. Chu, R. Bell, S. Bernabei, A. Cavallo, S. Guharay, W. Hooke, J. Hosea, F. Jobes, E. Mazzucato, D. McNeil, E. Meservey, R. Motley, J. Stevens, and S. Von Goeler, Nuclear Fusion, **26** , 666 (1986).

[47]D.J. Campbell, R.D. Gill, C.W. Gowers, J.A. Wesson, D.V. Bartlett, C.H. Best, S. Coda, A.E. Costley, A. Edwards, S.E. Kissel, M.M. Niestadt, H.W. Piekaar, R. Prentice, R.T. Ross, and B.J.D. Tubbing, Nuclear Fusion, **26**, 1085 (1986).

[48]TFTR Group, in *Plasma Physics and Controlled Nuclear Fusion Research 1986*, Proceedings of the 11th International Conference, Kyoto (IAEA, Vienna, 1987), Vol. 1, p. 421.

[49]JT-60 Team, in *Plasma Physics and Controlled Nuclear Fusion Research 1986*, Proceedings of the 11th International Conference, Kyoto (IAEA, Vienna, 1987), Vol. 1, p. 217.

[50]A.W. Edwards, D.J. Campbell, W.W. Engelhardt, H. -V. Fahrbach, R.D. Gill, R.S. Granetz, S. Tsuji, B.J.D. Tubbing, A. Weller, J. Wesson, and D. Zasche, Physical Review Letters, **57**, 210 (1986).

[51]D.J. Campbell, P.A. Duperrex, A.W. Edwards, R.D. Gill, C.W. Goweres, R. Granetz, M. Hugon, P.J. Lomas, N. Lopes-Cardozo, M. Malacarne, M.F. Nave, D.C. Robinson, F.C. Schüller, P. Smeulders, J.A. Snipes, P.E. Stott, G. Tonetti, B.J. Tubbing, A. Weller, and J.A. Wesson, in *Plasma Physics and Controlled Nuclear Fusion Research 1986*, Proceedings of the 11th International Conference, Kyoto (IAEA, Vienna, 1987), Vol. 1, p. 433.

[52]A.F. Danilov, Yu.N. Dnestorvskii, D.P. Kostomarov, and A.M. Popov, Soviet Journal of Plasma Physics, **2**, 167 (1976).

[53]A. Sykes and J.A. Wesson, Physical Review Letters, **37**, 140 (1976).

[54]B.V. Waddell, M.N. Rosenbluth, D.A. Monticello, and R.B. White, Nuclear Fusion, **16**, 528 (1976).

[55]R.E. Denton, J.F. Drake, R.G. Kleva, and D.A. Boyd, Physical Review Letters, **56**, 2477 (1986).

[56]J.A. Wesson, P. Kirby, and M.F. Nave, in *Plasma Physics and Controlled Nuclear Fusion Research 1986*, Proceedings of the 11th International Conference, Kyoto (IAEA, Vienna, 1987), Vol. 2, p. 3.

[57]D. Biskamp and H. Welter, in *Plasma Physics and Controlled Nuclear Fusion Research 1986*, Proceedings of the 11th International

Conference, Kyoto (IAEA, Vienna, 1987), vol. 2, p. 11.

[58]A.Y. Aydemir, Physical Review Letters, **59**, 649 (1987).

[59]R.G. Kleva, J.F. Drake, and R.E. Denton, Physics of Fluids, **30**, 2119 (1987).

[60]K. Yamazaki and G.L. Schmidt, in Proceedings of the Sixth International Conference on Plasma Surface Interaction in Controlled Fusion Devices, Nagoya, 1984.

[61]F. Karger, K. Lackner, G. Fussman, B. Cannici, W. Engelhardt, J. Gernhardt, E. Glock, D.E. Groening, O. Klüber, G. Lisitano, H.M. Mayer, D. Meisel, P. Morandi, S. Sesnic, F. Wagner, and H.P. Zehrfeld, in *Plasma Physics and Controlled Nuclear Fusion Research 1976*, Proceedings of the 6th International Conference, Berchtesgaden (IAEA, Vienna, 1977), Vol. 1, p. 267.

[62]S.V. Mirnov and I.B. Semenov, in *Plasma Physics and Controlled Nuclear Fusion Research 1976*, Proceedings of the 6th International Conference, Berchtesgaden (IAEA, Vienna, 1977), Vol. 1, p. 291.

[63]Equipe TFR, Nuclear Fusion, **17**, 1283 (1977).

[64]D.B. Albert and A.H. Morton, Nuclear Fusion, **17**, 863 (1977).

[65]N.R. Sauthoff, S. von Goeler, and W. Stodiek, Nuclear Fusion, **18**, 1445 (1978).

[66]K. Toi, S. Itoh, K. Kadota, K. Kawahata, N. Noda, K. Sakurai, K. Sato, S. Tanahashi, and S. Yasue, Nuclear Fusion, **19**, 1643 (1979).

[67]K.M. McGuire and D.C. Robinson, Physcial Review Letters, **44**, 1666 (1980).

[68]DIVA Group, Nuclear Fusion, **20**, 271 (1980).

[69]S.V. Mirnov, Soviet Journal of Plasma Physics, **7**, 436 (1981).

[70]F. Alladio, G. Bardotti, R. Bartiromo, G. Bracco, F. Bombarda, G. Buceti, P. Buratti, E. Caiaffa, R. Cesario, F. Crisanti, R. DeAngelis, F. DeMarco, M. DePretis, D. Frigione, R. Gianella, M. Grolli, R. Iacono, S. Mancuso, M. Marinucci, G. Mazzitelli, F. Orsitto, V. Pericoli-Ridolfini, L. Pierone, S. Podda, G.B. Righetti, F. Romanelli, D. Santi, S.E. Segre, A.A. Tuccillo, O. Tudisco, G. Vlad, and V. Zanza, Nuclear Fusion, **26**, 11 (1986).

[71]A.D. Cheetham, S.M. Hamberger, J.A. How, H. Kuwahara, A.H. Morton, L.E. Sharp, and C.F. Vance, in *Plasma Physics and Controlled Nuclear Fusion Research 1984*, Proceedings of the 10th International Conference, London (IAEA, Vienna, 1985), Vol. 1, p. 337.

[72]D.C. Robinson and K. McGuire, Nuclear Fusion, **19**, 115 (1979).

[73]J.A. Snipes, D.J. Campbell, P.S. Haynes, T.C. Hender, M. Hugon, N. Lopez Cardozo, and F.C. Schuller, in Proceedings of the Fourteenth European Conference on Controlled Fusion and Plasma Physics, Madrid, 1987 (EPS, Geneva, 1987), Vol. 11D, Part 1, p. 69.

[74]S. Tsuji, Y. Nagayama, K. Miyamoto, K. Kawahata, N. Noda, and S. Tanahashi, Nuclear Fusion, **25**, 305 (1985).

[75]K. Makishima, T. Tominaga, H. Tohyama, and S. Yoshikawa, Physical Review Letters, **36**, 142 (1976).

[76]I.H. Hutchinson, Physical Review Letters, **37**, 338 (1976).

[77]L. Giannone, R.C. Cross, and I.H. Hutchinson, Nuclear Fusion, **27**, 2085 (1987).

[78]J.A. Goetz, R.N. Dexter, and S.C. Prager, Physical Review Letters, (submitted 1990).

[79]K. Toi, K. Sakurai, S. Tanahashi, S. Yasue, Nuclear Fusion, **22**, 465 (1982).

[80]M. Okabayashi, K. Bol, K. McGuire, and H. Maeda, Bulletin of the American Physical Society, **25**, 928 (1980).

[81]P. Couture and K. McGuire, PPPL-2380 (1986).

[82]M. Murakami, J.D. Callen, and L.A. Berry, Nuclear Fusion, **16**, 347 (1976).

[83]M. Nagami, H. Toshida, K. Shinya, G.L. Jahns, H. Yokomizo, M. Shimada, K. Ioki, S. Izumi, and A. Kitsunezaki, Nuclear Fusion, **22**, 409 (1982).

[84]TFR Group, Nuclear Fusion, **24**, 784 (1984).

[85]K.B. Axon, W.H.M. Clark, J.G. Cordey, M. Cox, S.J. Fielding, R.D. Gill, J. Hugill, P. Lomas, J.W.M. Paul, B.A. Powell, R. Prentice, D.F.H. Start, D.D.R. Summers, and P. Thomas, in *Plasma Physics and Controlled Nuclear Fusion Research 1980*, Proceedings of the 8th International Conference, Brussels (IAEA, Vienna, 1981), Vol. 1, p. 413

[86]JET Team, in *Plasma Physics and Controlled Nuclear Fusion Research 1986*, Proceedings of the 11th International Conference, Kyoto (IAEA, Vienna, 1987), Vol. 1, p. 31.

[87]B.B. Kadomtsev and O.P. Pogutse, Soviet Physics JETP, **38**, 283 (1974).

[88]M.N. Rosenbluth, D.A. Monticello, M.N. Rosenbluth, and R.B. White, Physics of Fluids, **19**, 1987 (1976).

[89]R.B. White, D.A. Monticello, M.N. Rosenbluth, and B.V. Waddell, Physics of Fluids, **20**, 800 (1977).

[90]R.B. White, D.A. Monticello, and M.N. Rosenbluth, Physical Review Letters, **39**, 1618 (1977).

[91]J.F. Drake and R.G. Kleva, Physical Review Letters, **53**, 1465 (1984).

[92]R.G. Kleva, J.F. Drake, and D.A. Boyd, Physics of Fluids, **29**, 475 (1986).

[93]A. Sykes and J.A. Wesson, Physical Review Letters, **44**, 1215 (1980).

[94]B.V. Waddell, B. Carreras, H.R. Hicks, J.A. Holmes, and D.K. Lee, Physical Review Letters, **41**, 1386 (1978).

[95]B.V. Waddell, B. Carreras, H.R. Hicks, and J.A. Holmes, Physics of Fluids, **23**, 896 (1979).

[96]B. Carreras, H.R. Hicks, J.A. Holmes, and B.V. Waddell, Physics of Fluids, **23**, 1811 (1980).

[97]D. Biskamp and H. Welter, in *Plasma Physics and Controlled Nuclear Fusion Research 1982*, Proceedings of the 9th International Conference, Baltimore (IAEA, Vienna, 1983), Vol. 3, p. 373.

[98]A. Bondeson, Nuclear Fusion, **26**, 929 (1986).

[99]R. Izzo, D.A. Monticello, W. Park, J. Manickam, H.P. Strauss, R. Grimm, and K. McGuire, Physics of Fluids, **26**, 2240 (1983).

[100]M.F. Turner and J.A. Wesson, Nuclear Fusion, **22**, 1069 (1982).

[101]K.I. Hopcraft and M.F. Turner, Physical Review Letters, **56**, 2372 (1986).

[102]J.J. Ellis, K.McGuire, R. Peacock, D.C. Robinson, and I. Stares, in *Plasma Physics and Controlled Nuclear Fusion Research 1980*, Proceedings of the 8th International Conference, Brussels (IAEA, Vienna, 1981), Vol. 1, p. 731.

[103]S.J. Fielding, J. Hugill, G.M. McCracken, J.W.M. Paul, R. Prentice, and P.E. Stott, Nuclear Fusion, **17**, 1382 (1977).

[104]M.F.F. Nave and J.A. Wesson, in Proceedings of the Fourteenth European Conference on Controlled Fusion and Plasma Physics, Madrid, 1987, (EPS, Geneva, 1988), Vol. 11D, Part III, p. 1103.

[105]A. Bondeson, Ecole Polytechnique Federale De Lausanne - Suisse , Report LRP 335/87 (1987).

[106]Z. Yoshida, K. Okano, Y. Seike, M. Nakanishi, M. Kikuchi, N. Inoue, and T. Uchida, in *Plasma Physics and Controlled Nuclear Fusion Research 1982*, Proceedings of the 9th International Conference, Baltimore (IAEA, Vienna, 1983), Vol. 3, p. 273.

[107]T. Edlington, J.L. Luxon, T.N. Todd, and D.C. Robinson, in *Plasma Physics and Controlled Nuclear Fusion Research 1982*, Proceedings of the 9th International Conference, Baltimore (IAEA, Vienna, 1983), Vol. 3, p. 241.

[108]TFR Group and J.A. Hoekzema, Proceedings of the 5th International Workshop on Electron Cyclotron Emission and Electron Cyclotron Heating, San Diego, 1985, p. 154.

Chapter 3

Experimental Apparatus and Diagnostics

The experiments described in this thesis were conducted on the Tokapole II tokamak.[1] Tokapole II (Figure 3.1) is a four node poloidal divertor tokamak operating at the University of Wisconsin – Madison Physics Department since 1978. A complete description of the engineering and physics considerations of the device can be found elsewhere.[2,3] The features of Tokapole II that are relevant to this work are presented here along with the changes accomplished during the upgrade of 1987.

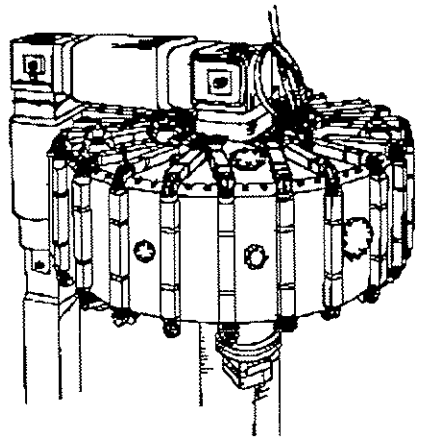

Figure 3.1
Tokapole II tokamak

III.A. Tokapole II

The vacuum vessel is an aluminum torus with a major radius of 50 cm and a 44 cm square cross section (Figure 3.2). Since the walls are 3 cm thick, there are insulated breaks ("gaps") in both the poloidal and toroidal directions to allow the externally driven magnetic fields to penetrate. There are four solid chromium-copper toroidal rings located inside the vacuum vessel, each supported at three locations by insulated Inconel rods. The divertor is formed by inductively driving these rings. The position of the rings can be adjusted vertically ± 5 mm to position and shape the plasma. The installation of these Inconel ring supports was one of the prime objectives of the Tokapole II upgrade.[4] The new ring supports allow larger ring currents to be driven and a greater range of operating parameters for the poloidal field system.

Diagnostic access is provided by ports on the outside wall along the midplane and on the lid and floor along the midcylinder. These ports have valves attached through which probes can be inserted into the machine without breaking vacuum. Many of these probe ports can swivel up to 25° in all directions which allows access to a large fraction of the volume of the vessel.

The vacuum volume of Tokapole II is approximately 610 liters and the vacuum surface area is just over 5.5 square meters. The vacuum is maintained by pumping with a 1500 liter/sec turbomolecular pump. Additional pumping can be achieved with titanium gettering of the vacuum surface. Typical base pressures are in the low 10^{-7} torr range. There is a quadrupole residual gas analyzer to monitor vacuum quality.

The primary method of wall and probe conditioning is daily pulsed discharge cleaning, although glow discharge cleaning is used after machine venting.

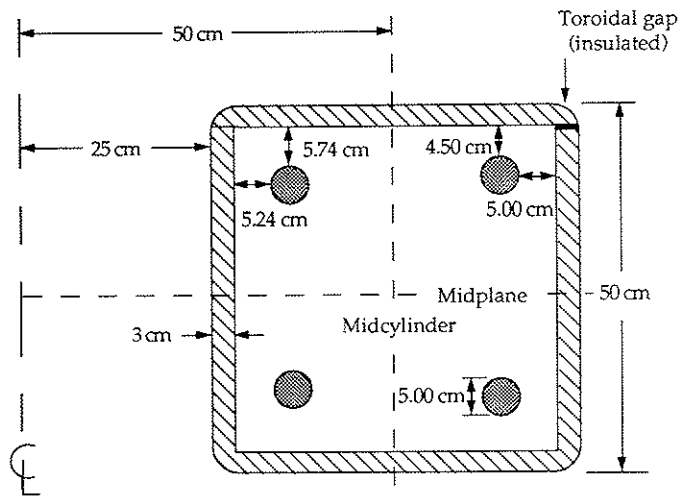

Figure 3.2
Tokapole II cross section showing ring position

The toroidal field is generated by 96 turns of 4/0 wire wound poloidally around the torus. The windings are separated into 4 groups of 24 turns which are driven in parallel directly by a 78 mF, 5 kV capacitor bank switched by a class E ignitron. This bank is configured as a two section pulse forming network in order to flatten the waveform.[5] This bank is also passively crowbarred by another class E ignitron wired to automatically trigger when there is zero voltage on the capacitor bank.

This arrangement gives a toroidal field waveform which is reasonably flat for the duration of the discharges studied. The toroidal field system has the capability of producing 8 kgauss on the axis of the torus but is generally run at less than 5.5 kgauss.

The toroidal current in the rings and the plasma is inductively driven by an iron core transformer linking the torus (the iron core has a total flux swing of 0.15 volt-seconds). The primary of the transformer is driven by a 7.5 mF, 5 kV capacitor bank switched through a class E ignitron and can be run with either a 40 : 1 or 80 : 1 turns ratio. There is also a 0.96 F, 450 V capacitor bank connected by a diode stack as a power crowbar to clamp the poloidal gap voltage at the peak of the current waveform. There is a removable damping resistor in the circuit. Greater peak currents can be achieved without the damping resistor, but longer discharges are more easily obtained with it in. Total ring currents range from 200 to 500 kiloamps while plasma currents range from 10 to 100 kiloamps depending on the configuration of the poloidal field system.

When the rings alone are driven an octupole vacuum poloidal field is produced. When plasma current is driven toroidally through the octupole null, the four node poloidal divertor tokamak configuration is produced. Numerically generated poloidal flux contours for both these configurations are shown in Figure 3.3. Since the ring and plasma currents are in the same direction, there are nulls ("x-points") in the poloidal field produced by these currents. There is also a surface (the separatrix) which separates topologically distinct flux contours; those which enclose a single conductor (private flux) and those which enclose

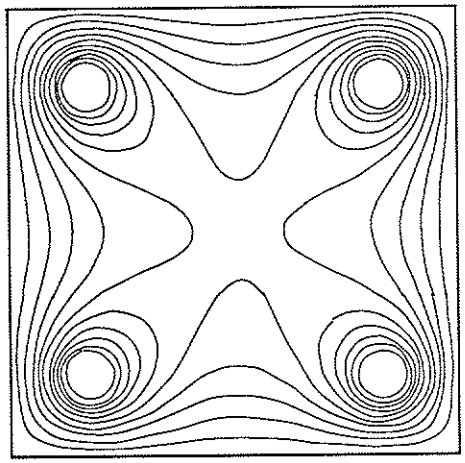

Figure 3.3(a)
Vacuum poloidal flux plot showing octupole field (ring currents only)

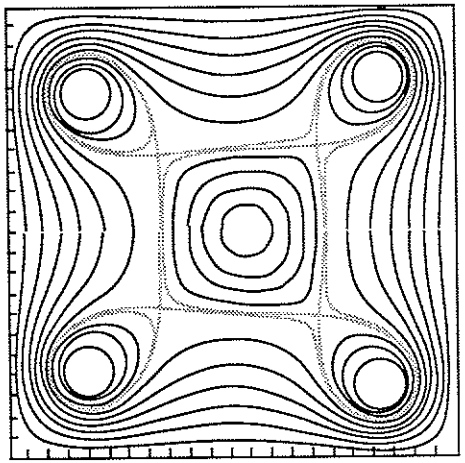

Figure 3.3(b)
Poloidal flux plot for a tokamak discharge in Tokapole II

all 5 conductors (common flux). The exact location of the x-points and separatrix depends on the ratio of current in the divertor rings to that in the plasma and the exact positioning of the divertor rings.

Tokapole II has stainless steel limiter plates on all four walls at one toroidal azimuth. The plates on the inner and outer walls can be inserted beyond the separatrix while the plates on the lid and the floor can be inserted only part way to the separatrix. The region of flux surfaces inside the separatrix is referred to as the "central current channel" and the region outside the separatrix is known as the "scrapeoff region". In the "material limiter" configuration, the central current channel is defined by the limiter plates and in the "magnetic limiter" configuration, the central current channel is defined by the magnetic separatrix.[6] Thus these limiter plates allow controlled variation of the plasma boundary conditions and interaction with the magnetic separatrix.

Plasma formation in Tokapole II is essentially like that of most other tokamaks and has been described in detail by Groebner[3]. There are several review articles[7,8,9] on tokamak operation that describe general characteristics of startup. Tokapole II operates with hydrogen gas, puffed through a fast piezoelectric valve 16.66 msec before the triggering of the poloidal field. This timing is optimized for the diffusion of the neutrals around the torus to a typical fill pressure of $3 - 10 \times 10^{-4}$ torr. Additional gas is puffed in via feedback control of the piezoelectric valve for refueling purposes. Preionization of the hydrogen is accomplished by a nude fast ion gauge (a free electron source), 100 W of cw S-band (2.45 GHz), and ten

kW of pulsed X-band (9.0 GHz) or K-band (16.5 GHz), depending on the toroidal field strength. The toroidal field is initiated nine msec (typically) before the poloidal field in order for the waveform to reach its maximum value and remain nearly constant for the duration of the experiment. Figure 3.4 shows a complete timing diagram for the startup of Tokapole II.

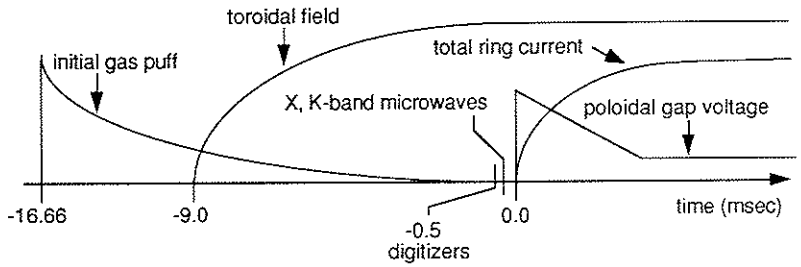

Figure 3.4
Timing diagram for a typical Tokapole II pulse. The waveforms shown are for illustration purposes only.

Data acquisition is CAMAC based with LeCroy model 8210, DSP Technologies TRAQ system models 4012 and 4012A, and DSP model 2001A digitizers along with their associated memory modules. The digitizers are usually triggered 0.5 msec before the poloidal field pulse in order to have sufficient sampling for baseline information. The Model Data System (MDS) developed at the Massachusetts Institute of Technology is the software used to manage the CAMAC which is optically interfaced with a MicroVax II used for data storage and analysis. Data analysis is accomplished with VAXFORTRAN and the Interactive Data

Language (IDL) from Research Systems Inc.

III.B. General Diagnostics

Discharge characteristics that are routinely measured by diagnostic devices available on Tokapole II are the poloidal gap voltage, the average density, the averaged edge ion saturation current, and the average toroidal field on the axis of the torus. Discharge characteristics that are determined from measured data include the plasma current and the ring current.

The voltage across the poloidal gap, V_{pg}, is measured using a single turn flux loop around the iron core. The line-averaged electron density on a chord through the midcylinder of the machine is measured using a 70 GHz digital microwave interferometer. A complete description of the workings of the interferometer is contained in Reference 10. The average ion saturation current in the region between a ring and the wall is measured using a double Langmuir probe. The average toroidal field is determined by integrating the toroidal gap voltage to obtain the total toroidal flux and then dividing by the cross-sectional area of the torus. This technique is documented in Reference 11.

A reasonable model of the plasma current profile is used to determine the plasma current and ring current from V_{pg} and the primary current I_{pr} (measured with a 0.001 Ω resistive shunt in series with the primary windings).[12] This is necessary because the divertor currents are inductively driven rather than directly driven and a nonperturbing measurement is not possible. The model used assumes that in some

appropriate flux space average, the plasma current can be treated as if it is all concentrated at the axis of the torus (at the octupole null). Using this assumption and the circuit model shown in Figure 3.5[13] the plasma and ring currents are given by:

$$I_p = \frac{N}{\alpha} I_{pr} - \frac{1}{\alpha L_r} \int V_{pg} dt + \frac{1}{\alpha L_r} \int I_r R_r dt \qquad (3.1)$$

$$I_r = N I_{pr} - I_p \qquad (3.2)$$

where α = private flux/common flux in the absence of plasma (~ 0.5), N is the primary turns ratio (typically 40), I_p is the plasma current in kamps, I_r, R_r, and L_r are the ring current in kamps, resistance in ohms, and inductance in henrys respectively, and V_{pg} is in volts. These equations are solved by an analog circuit and have been shown to agree with ring Rogowski measurements to within 25 percent.[14,15]

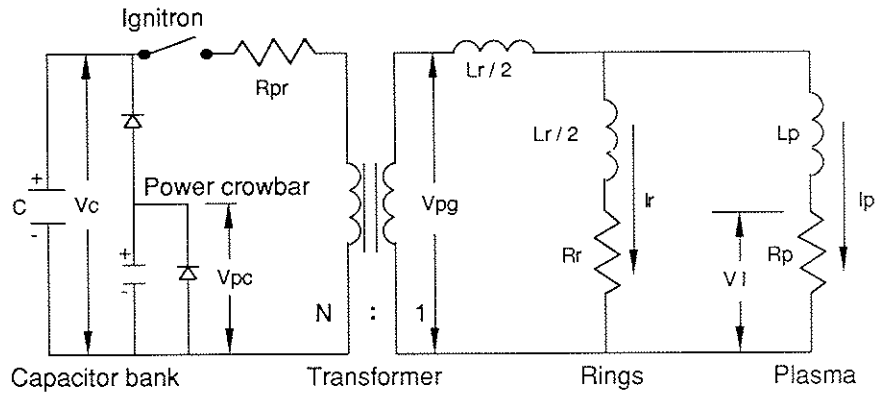

Figure 3.5
Circuit model from Reference 13 used to model Tokapole II

Once I_p, I_r, and V_{pg} are known the following quantities are calculated: plasma minor radius, "effective edge safety factor", resistive loop voltage, Ohmic input power, average electron conductivity temperature, and the global energy confinement time. If the plasma current distributes itself uniformly within the separatrix, then the plasma radius, a, is given by:[16]

$$a = 17.3 \left| I_p / (I_p + I_r) \right|^{1/4} \qquad (3.3)$$

where a is in centimeters and is equivalent to the radius of a circle with the same cross sectional area as the area inside the separatrix. If this circle of radius a with uniform current density is centered on the axis, then the "effective edge safety factor" q_a is:

$$q_a = 10^{-4} a^2 B_t / I_p \qquad (3.4)$$

where B_t is the toroidal field in kgauss. The resistive loop voltage, which is the voltage around a contour encircling the torus toroidally at the axis, can be derived using the circuit model of Figure 3.5. Experimental measurements of plasma and ring inductance give:

$$V_l = 0.5 \left(1 + \frac{t}{75} \right) V_{pg} + 0.0045 \left(1 - \frac{t}{37} \right) I_r - 2.3 \frac{dI_p}{dt} \frac{1}{\sqrt{a}} \qquad (3.5)$$

where t is the time in msec after the start of the discharge. This expression is only accurate for low frequency changes in the loop voltage because it does not take into account high frequency current profile changes. The Ohmic input power is given by:

$$P_{oh} = I_p V_l \qquad (3.6)$$

The average electron conductivity temperature measured in electron volts (eV) can be inferred from I_p, V_l, and the plasma radius:

$$T_e = 376 \left(\left| I_p / V_l \right| / a^2 \right)^{2/3} \qquad (3.7)$$

where Spitzer resistivity[17] and no impurities, $Z_{eff}=1$, is assumed. The global energy confinement time is determined by assuming a steady state which gives:

$$\tau_e = 0.144 \langle n_e T_e \rangle / P_{oh} \qquad (3.8)$$

where the entire volume of stable confinement is used and thus τ_e represents a total machine confinement time. There are many approximations involved in the derivation of Equations (3.3) to (3.8) as discussed in References 12 and 15. Nevertheless these parameters allow observation of gross changes of plasma behavior as conditions vary.

Soft x-ray (SXR) radiation is used as a diagnostic for the central plasma conditions of Tokapole II. Radiation in plasmas in the SXR region comes primarily from sources that are strongly dependent on electron temperature,[18] so that even though a collimated detector averages over a chord, the detected signal comes primarily from the hottest point along the chord. The central electron temperature is approximately 100 eV.[3] At this temperature line radiation is expected to be the primary component of the SXR signal. Impurity doping experiments[19] indicate that light impurities account for < 20% of the SXR radiation. At 100 eV the intensity of radiation from metals in Tokapole II[19,20] varies as

$$I_{SXR} \sim n_e n_i \exp(-280 / T_e) \qquad (3.9)$$

where I_{SXR} is the intensity of the soft X-ray radiation, n_e is the electron density, and n_i is the density of the i^{th} impurity charge state.

Surface barrier diodes with polypropylene filters are used for SXR detection on Tokapole II. This combination allows for sensitivity to

photon energies of about 60 - 300 eV. The diodes are operated in current mode and are biased to -5 V to improve the frequency response which is approximately 300 kHz. The detector systems consist of a seven chord poloidal array along the outside wall and several movable detectors that can be positioned at various locations around the torus. The detectors in the poloidal array are separated by 3.18 cm and view a spot size at the midcylinder of ~2 cm. The central chord SXR signal is a good diagnostic for following changes in the central current channel's temperature and density.

Filtered photomultipliers are used to monitor impurity signals. The lines monitored regularly are C III (464.7 nm), N III (450.9 nm), O III (376.3 nm), and Cu I (324.7 nm). These lines give a good indication of the overall cleanliness of the discharge. Other filters exist to look at selected impurities but are not regularly monitored.

III.C. Magnetic Probes and Analog Integrators

In addition to SXR emissivity measurements, the basic information needed to perform this research is a knowledge of the internal magnetic field structure. The instrument used to gain this knowledge is the "b-dot" probe – so named because the output is proportional to the time derivative of the magnetic flux at the probe tip. A thorough discussion of magnetic probe techniques for plasma diagnostics are given in References 21, 22, and 23.

The magnetic probes used in this work have been developed

specifically for this research. Previous measurements of the internal magnetic fields in Tokapole II[6,24,25] were done with what is known as a standard Tokapole II magnetic probe. These measurements were performed in discharges with $q_a < 1$ and could not be done at $q_a > 1$ due to probe perturbation of the discharge. To be able to measure the internal magnetic fields in $q_a > 1$ discharges a less perturbing probe was needed. The basic design for what became known as a "mini-probe" is accredited to Professor R.N. Dexter. Many modifications were realized before a final, acceptable magnetic "mini-probe" was put to reliable use in Tokapole II.

The probes used consist of two orthogonal magnetic coils, oriented to measure the magnetic fields parallel and perpendicular to the probe axis. The coils are wound on alumina forms (two-bore rods turned down to an "H" cross section) with 48 gauge HML coated wire (usually eight to ten turns). Typical coil resistances are 50 ohms and typical effective coil areas are twenty square millimeters. The coils are encased in #29 Sauereisen cement and binder for protection from abrasion and heat. Structural support and electrostatic shielding is provided by a stainless steel tube (0.050 inch outside diameter, 0.008 inch thick wall) into which the encased coils are inserted.

A boron nitride sheath is used for particle shielding and heat deposition. These sheaths are machined from a solid rod of 1/4 inch, combat grade boron nitride. A 0.052 inch hole is drilled down the center and the rod is then turned down to an outer diameter of less than 0.080 inches (depending on the luck of the machinist that day). The tube

containing the coils is inserted into this sheath.

The main body of the probe is a 1/4 inch outer diameter, 0.064 inch thick seamless stainless steel tube. The sheath containing the coils is attached to the probe body with a collet/nut assembly. The vacuum seal is made at the back end of the probe with a breakout pot and vacuum feedthrough BNC connectors. An assembly drawing of these probes is shown in Figure 3.6.

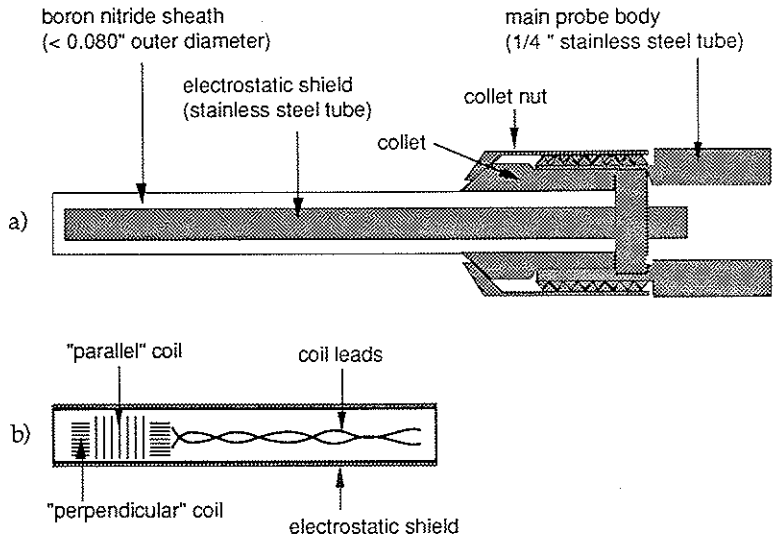

Figure 3.6

Assembly drawing for a magnetic "mini-probe" used in this research, showing a) the support structure of the probe and b) the coils inside the electrostatic shield. The vacuum seal is made on the main probe body and is not shown in this drawing.

The output of a magnetic pickup coil is given by:

$$V = -\frac{d\Phi}{dt} = -\frac{d}{dt}\int \vec{B} \cdot \vec{dS} = -A_{eff}\frac{d< B >}{dt} \qquad (3.10)$$

where Φ is the magnetic flux linked by the coil, $\vec{B}$ is the magnetic field at the coil, $\vec{dS}$ is the element of coil area, A_{eff} is the effective area of the coil, and $< B >$ is the average magnetic field over the coil area. For an ideal coil, $A_{eff} = NA$ where N is the number of turns and A is the area/turn. Due to imprecision in winding and attenuation of the signal due to the finite thickness of the electrostatic shield, the effective area does not obey such a simple relation. In addition, A_{eff} has frequency dependence. These effects can be accounted for by assuming an ideal coil during calibration and including all the aforementioned effects in $A_{eff}(\omega)$. Probe calibration is accomplished with a Helmholtz coil set that produces a known magnetic field. Coils are calibrated from near d.c. to 300 kHz and can generally be represented by a frequency independent A_{eff} at these frequencies.

In order to obtain the magnetic fields from the signals output by the probes Equation (3.10) must be integrated. This is accomplished with a low drift, low offset, auto-zeroing active integrator designed by J.S. Sarff.[26] Figure 3.7 shows this integrator circuit. The magnetic field measured is the average field seen by the coil of effective area A_{eff} and is given by:

$$< B > = -\frac{1}{A_{eff}}\int V_{pr}\, dt = \frac{|V_i|}{G_i\, A_{eff}} \qquad (3.11)$$

where V_{pr} is the output of the probe [given by Equation (3.10)], V_i is the output of the integrator, and G_i is the gain of the integrator (approximately 10^4 for this model of integrator).

The integration bandwidth of the circuit of Figure 3.7 is 0.0016 Hz–700 kHz, and the effective integration time constant is variable over the range 1–100 μsec. Integrator drift errors are eliminated by an auto-zeroing feature that maintains an input offset voltage of less than 0.5 μV between the integrating amplifier inputs. The output is switchable between the integral and the reference voltage which allows for ample digitization of the desired signal. There is also a buffered input for monitoring the coil signal without disturbing the integration. This feature is used to simultaneously obtain magnetic field and magnetic field fluctuation information.

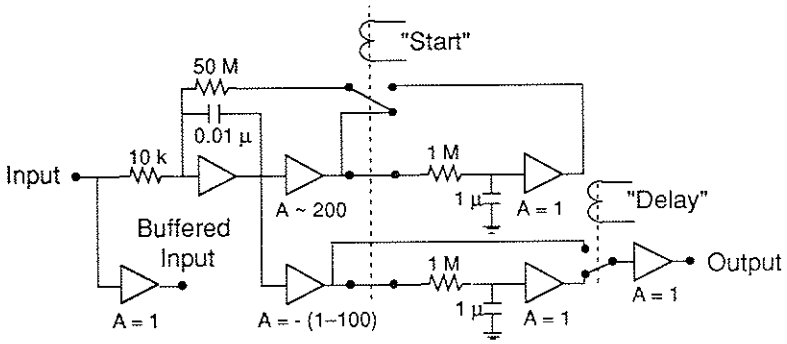

Figure 3.7
Active analog integrator circuit with auto-zeroing and reference voltage memory features used in this research (from Reference 26).

REFERENCES

[1]A.P. Biddle, R.N. Dexter, R.J. Groebner, D.T. Holly, B. Lipschultz, M.W. Phillips, S.C. Prager, and J.C. Sprott, Nuclear Fusion, **19** , 1509 (1979).

[2]J.C. Sprott and T.W. Lovell, University of Wisconsin Plasma Studies, PLP 744 (1978).

[3]R.J. Groebner, Ph.D. Thesis, University of Wisconsin (1979).

[4]J.C. Sprott, University of Wisconsin Plasma Studies, PLP 962 (1985).

[5]M.A. Lapointe, Ph.D. Thesis, University of Wisconsin (1990).

[6]R.A. Moyer, Ph.D. Thesis, University of Wisconsin (1988).

[7]L.A. Artsimovich, Nuclear Fusion, **12**, 215 (1972).

[8]H.P. Furth, Nuclear Fusion, **15**, 487 (1975).

[9]J. Sheffield, Proceedings of the IEEE, **69**, 885 (1981).

[10]H.R. Garner, University of Wisconsin Plasma Studies, PLP 833 (1981).

[11]J.S. Sarff, University of Wisconsin Plasma Studies, PLP 1034 (1988).

[12]J.C. Sprott, University of Wisconsin Plasma Studies, PLP 889 (1983).

[13]J.C. Sprott, University of Wisconsin Plasma Studies, PLP 777 (1979).

[14]N.S. Brickhouse, Ph.D. Thesis, University of Wisconsin (1984).

[15]S.C. Prager, J.C. Sprott, T.H. Osborne, and K. Miller, University of Wisconsin Plasma Studies, PLP 756 (1978).

[16]J.S. Sarff, University of Wisconsin Plasma Studies, PLP 1003 (1987).

[17]L. Spitzer, *Physics of Fully Ionized Gases*, John Wiley and Sons, (1962).

[18]S. von Goeler, *Diagnostics for Fusion Experiments* (Proceedings of the Course, Varenna, 1978), Edited by E. Sindoni and C. Wharton, (Pergamon Press, Oxford, 1979) pp. 79 - 109.

[19]R.J. Groebner and R.N. Dexter, University of Wisconsin Plasma Studies, PLP 770 (1978).

[20]G.M.McCracken and P.E. Stott, Nuclear Fusion, **19**, 889 (1979).

[21]R.H. Lovberg, Annals of Physics (New York), **8**, 311 (1959).

[22]R.H. Lovberg, *Plasma Diagnostic Techniques*, Edited by R.H. Huddlestone and S.L. Leonard, (Academic Press, Inc., New York, 1965), pp. 69 - 112.

[23]W. Botticher, *Plasma Diagnostics*, Edited by W. Lochte-Holtgreven, (North Holland Publishing Co., Amsterdam, 1969), pp. 617-667.

[24]B. Lipschultz, Ph.D. Thesis, University of Wisconsin (1979).

[25]T.H. Osborne, Ph.D. Thesis, University of Wisconsin (1984).

[26]J.S. Sarff, Ph.D. Thesis, University of Wisconsin (1988).

Chapter 4

Plasma Characteristics and Experimental Method

The experiments described in this thesis were designed to measure the safety factor profile during major disruptions in Tokapole II. The characteristics of the discharges investigated and the features of major disruptions in Tokapole II will be presented in this chapter. Also, the experimental method followed will be outlined and the data analysis techniques will be discussed. A description of the plasma equilibrium that results from data obtained using the experimental method will be presented in this chapter. These include equilibrium poloidal field vectors, poloidal flux contours, the global safety factor profile and the toroidal current density profile in Tokapole II. The temporal evolution of these quantities throughout major disruptions is discussed in the next chapter.

IV.A. Plasma Characteristics

Tokapole II has the capability of operating over a wide range of parameters. The effective edge safety factor, q_a, can be varied from above four to well below one by lowering the toroidal field and changing the shape of the poloidal gap voltage waveform. This range of operating parameters leads to a variety of equilibria and disruptive instabilities.[1,2]

Sawteeth appear in all discharges but with differing characteristics over the range of q_a studied. Major disruptions occur in discharges with q_a greater than two when the central current channel is defined by the magnetic separatrix. When the central current channel is defined by limiter plates, major disruptions occur with q_a greater than 1.5.[2] Since the experiments described in this thesis involve measurement of the central safety factor during major disruptions in magnetic limiter discharges, only data for discharges with $q_a = 3$ will be presented.

IV.A.1 Global Characteristics of Plasmas with $q_a = 3$

Typical plasma parameters for the discharges investigated are listed in Table 4.1. These parameters are determined by the methods discussed in Section III.B. The electron temperature was determined by modelling the time evolution of oxygen line ratios[3] and the ion temperature was determined by Doppler broadening measurements[3] and charge exchange measurements.[4] The magnetic Reynolds number is expressed as $S = \tau_r/\tau_A$ where $\tau_r = a^2/\eta$ is the resistive diffusion time and $\tau_A = a\rho^{1/2}/B_p$ is the poloidal Alfvèn transit time.

The time evolution of the plasma current, the central chord SXR signal, the resistive loop voltage, the plasma radius, and q_a are plotted in Figure 4.1. The plasma current during the so called "flat-top" portion of the discharge is slowly decaying. This decay is due to the constant poloidal gap voltage driving the current and the mismatch between the plasma and ring resistances.

Table 4.1

Tokapole II Parameters for a Discharge with $q_a = 3$

Toroidal field	≥ 5.0 kGauss
Plasma current	10 - 15 kAmps
Plasma radius	~ 9 cm
Edge safety factor	2.5 - 3.0
Line averaged density	~ 6×10^{12} cm^{-3}
Electron temperature	~ 120 eV
Ion temperature	~ 40 eV
Magnetic Reynolds # ($S = \tau_r/\tau_A$)	~ 10^4
Energy confinement time	0.4 msec
Discharge duration	4 - 6 msec

Major disruptions appear as giant sawteeth on the central chord soft (XR) signal and are easily distinguished from sawtooth oscillations. Distinguishing characteristics are the amplitude, period, inversion and mode structure of the collapse.[2] The amplitude of a sawtooth on is approximately 30% of the central soft x-ray signal and that of

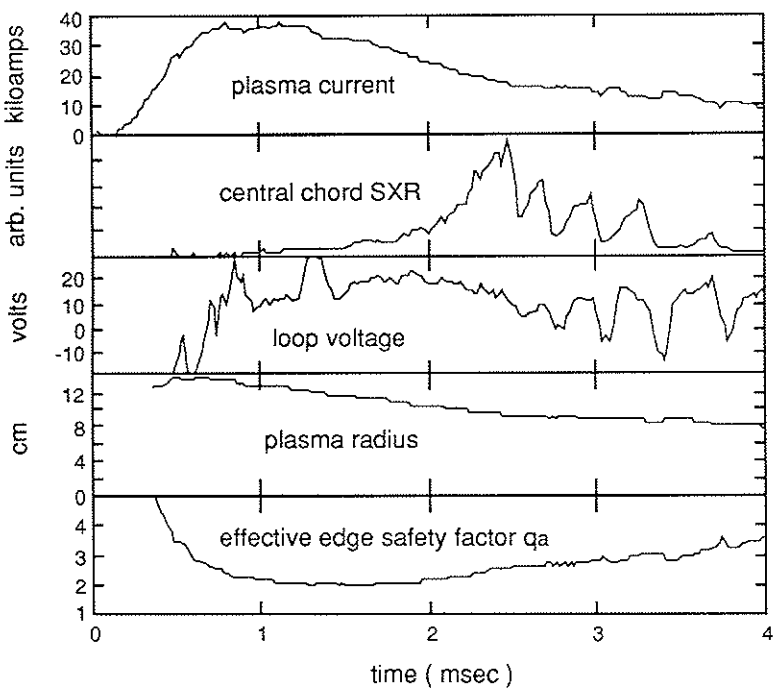

Figure 4.1
Plasma characteristics of a discharge with $q_a = 3$ used in this research. Major disruptions manifest themselves as giant sawteeth on the SXR signal, negative spikes on the loop voltage signal, and slight rises on the plasma current trace.

a major disruption is 80 - 100%. The period of sawtooth oscillations is 100 - 150 μsec and increases to 200 - 300 μsec for major disruptions. Inversion radii have been identified with mode rational surfaces; the q = 1 surface for sawtooth oscillations and the q = 2 surface for major disruptions. The (m,n) = (1,1) mode has been identified coincident with sawtooth

oscillations and a (2,1) mode with a (3,2) distortion has been seen together with major disruptions.

There is a slight rise in the plasma current coincident with a disruption and the change becomes more pronounced as the disruptions progress. The duration of the discharge is sensitive to impurity levels and will change the number of disruptions that occur. Negative spikes appear on the loop voltage trace at the time of a major disruption and are due to the lowered plasma inductance as discussed in Section II.C.1.b. The average plasma radius remains constant at approximately nine centimeters throughout the duration of the disruptions. There is a slight increase in the plasma radius coincident with the disruption which is difficult to discern due to the digitization rate used to obtain the data. The effective edge safety factor, q_a, is equal to 2.5 at the time the SXR signal begins to rise and is equal to 3.0 when the disruptions begin. For the remainder of this thesis, these plasmas will be referred to as discharges with $q_a = 3$.

The time evolution of the line averaged density, electron conductivity temperature, and global energy confinement time for the discharge of Figure 4.1 are plotted in Figure 4.2. The density is nearly constant at a value of 6×10^{12} cm^{-3} throughout the discharge. The electron conductivity temperature is approximately 60 eV during the startup of the discharge and increases to about 120 eV during the "flat-top" portion of the discharge. The temperature is determined from Equation (3.7) and uses a previously measured Z_{eff} of 2.5 - 3.[3] The ion temperature remains relatively constant at approximately 40 eV throughout the discharge. The

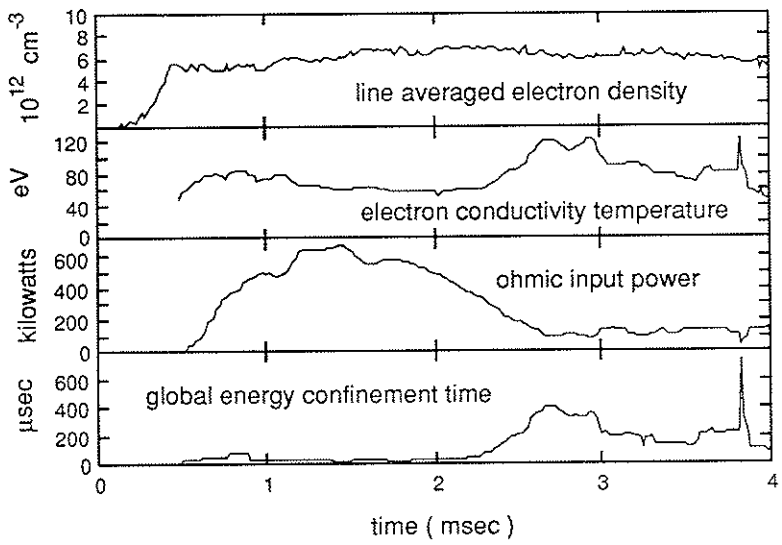

Figure 4.2
Additional plasma parameters for the discharge shown in Figure 4.1. The effects of the loop voltage spikes due to disruptions have been filtered out of the temperature and confinement time traces in order to show the low frequency behavior of these quantities.

ion distribution function is obtained on a shot–to–shot basis. Thus the temporal evolution of the ion temperature is not available and is not included in Figure 4.2. These discharges have a global energy confinement time of approximately 50 μsec during the startup phase of the discharge. This confinement time is so low because of the large loop voltage due to the ramping down of the plasma current. When the "flat-top" portion of the discharge is reached, the confinement time is approximately 400 μsec and decreases as the disruptions progress. The time traces of temperature,

Ohmic power, and confinement time have been filtered to remove the effect of the high frequency loop voltage spikes. This combination of low density and low temperature plasma allows probes to be used to diagnose the main current channel.

IV.A.2 Major Disruptions in Tokapole II

Magnetic and material limiter discharges display giant sawteeth on the SXR emissivity signals. These giant sawteeth have been identified as major disruptions. The striking difference between the two configurations is the termination of the discharge in the material limiter configuration. This termination arises from plasma contact with the inboard limiter.[2] The characteristics of major disruptions in magnetic limiter discharge will be discussed in the following paragraphs.

Major disruptions in the magnetic limiter configuration of Tokapole II manifest themselves as giant sawteeth which saturate prior to the fast collapse on the central chord SXR detector signal (see Figure 4.1). These giant sawteeth are remarkably regular despite the severity of the collapse whose amplitude can be up to 100% of the SXR signal. The period of the disruptions is 0.2 – 0.3 msec and remains constant throughout the discharge. Figure 4.3 shows a temporal and spatial evolution of the third disruption of Figure 4.1. The disruption occurs at 3.025 msec. The SXR signals shown were obtained from a discharge that is centered at y ~ +1 cm. By comparing the SXR precursor oscillation on chords on either side of the center, it is seen that these disruptions have an odd m > 1 character. The

collapse is nearly toroidally symmetric[2] and propagates inward in minor radius. The edge SXR chords rise sharply at or after the time of the central collapse, but not before.

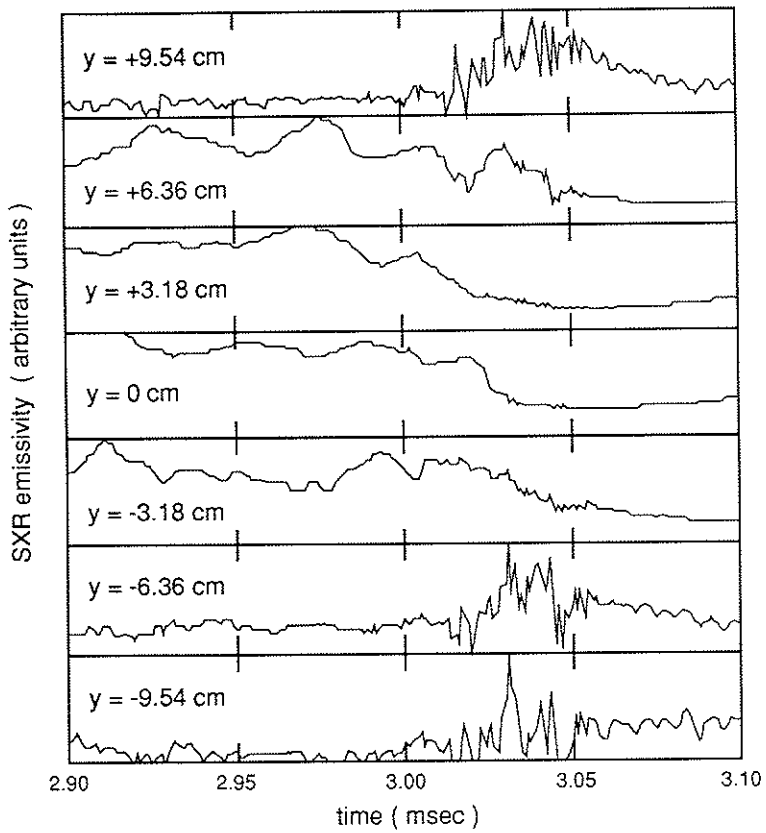

Figure 4.3
Expanded time view of the third major disruption of Figure 4.1 as seen by a poloidal array of SXR detectors. The vertical position of the horizontal chord viewed by each detector is denoted on the figure.

A profile of SXR emissivity before and after a major disruption is shown in Figure 4.4. The data from a swivelable SXR detector was analyzed 50 μsec before and 50 μsec after a disruption in order to obtain the profiles. The data has been averaged over 50 μsec to remove the effects of sawteeth and precursor oscillations. The emissivity profile before a disruption is very peaked. The small "shoulder" is probably due to the shot-to-shot variability of the data analyzed. It is seen that most of the SXR emissivity is lost after a disruption, with the profile becoming very broad. This profile after a disruption has rather large uncertainties due to the fact that most of the SXR signal is lost and thus the signal-to-noise ratio decreases dramatically.

The inversion radius for these major disruptions is 6.0 ± 0.4 cm, which is near but somewhat inside the divertor separatrix. Analysis of these discharges with $q_a = 3$ using an MHD equilibrium code suggests that the major disruption inversion radius is associated with the q = 2 rational surface.[5] It has also been shown that unphysically peaked current profiles are required to associate the q = 1 rational surface with the inversion radius of major disruptions.[1]

Mirnov loops placed in the plasma outside the separatrix detect bursts of magnetic activity that are correlated with major disruptions. Prior to the central chord collapse, a dominant (m,n) = (2,1) structure is detected on loops placed toroidally and poloidally around the torus. This precursor structure has a frequency of 30 - 40 kHz and grows exponentially before the collapse with a growth rate $\gamma_{2,1} = 2.4 \pm 0.1 \times 10^4$ sec^{-1}.[2] These oscillations are not purely sinusoidal but are distorted in a way consistent

with what would be expected if an m/n = 3/2 mode and m/n = 2/1 mode were rotating together with the same toroidal angular velocity in the electron diamagnetic drift direction.[6]

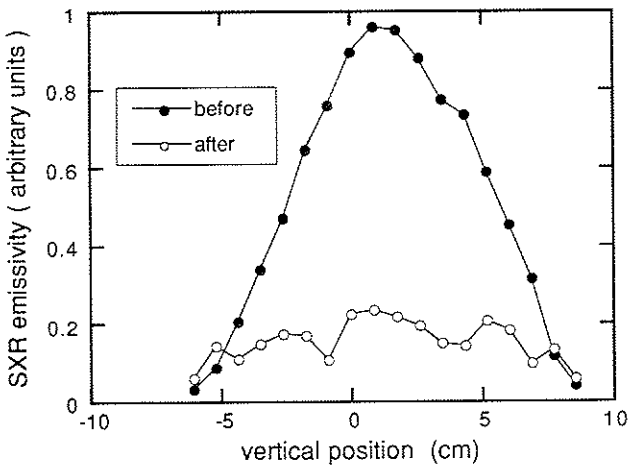

Figure 4.4
Soft x-ray emissivity profile 50 μsec before (solid circles) and 50 μsec after (open circles) a major disruption in a discharge with $q_a = 3$.

When the magnetic separatrix defines the central current channel, there is no abrupt current termination over the complete range of operating parameters. Abrupt current termination does occur in $q_a > 1.5$ discharges when limiters define the current channel. It has been determined by spectroscopic observation that contact with the inboard

limiter is the cause of current termination during a major disruption.[2] This contact with the limiter terminates the discharge through rapid cooling and impurity influx.

The importance of the inboard limiter can be understood in terms of standard major disruption behavior. The drop in poloidal beta and expulsion of poloidal flux along with the rapid expansion in minor radius of the plasma results in a post-disruption equilibrium position that is at a smaller major radius than the pre-disruption equilibrium position. The discharge will shift inward on a fast (Alfvèn) time scale unless a vertical field is present to maintain the equilibrium position. There is no actively coupled vertical field used in normal operation but the divertor ring fields do provide a passive vertical field. The large negative decay index of this vertical field leads to a small major radius shift, which is expected when the current profile is flattened in this divertor configuration.[7]

The characteristics of major disruptions in other tokamaks include abrupt thermal quench of the central current channel, a negative gap voltage spike preceding the disruption, initial plasma current rise during the thermal quench, and an exponentially growing (m,n) = (2,1) mode coupled to an odd m/even n mode just before disruption.[8,9,10,11] The similarity of the disruptions in Tokapole II to these characteristics suggest that the phenomena observed indeed are disruptions even though the current does not quench. This feature, along with the repetitive nature of the major disruptions, affords the opportunity to investigate a plasma with a pre-disruption and a post-disruption state.

IV.B. Experimental Method (Measurement of Ψ_p and $q(\Psi_p)$)

A determination of the flux-surface-averaged safety factor, $q(\Psi_p)$, requires a knowledge of the flux surfaces in the plasma which in turn requires measurement of the internal magnetic fields. The poloidal flux function is dependent on the poloidal magnetic field while the safety factor depends on the position in flux space along with the magnitude of the poloidal and toroidal magnetic fields. Thus, in order to obtain $q(\Psi_p)$ the internal magnetic fields must be measured. These fields are measured with magnetic probes which are inserted into the plasma. Each probe consists of two orthogonal magnetic coils, oriented to measure the magnetic fields parallel and perpendicular to the probe axis. Section III.C. describes in detail the probes and integrators used in this experiment. Figure 4.5 shows the data grid (18 cm x 18 cm with a step size of 2 cm) used for the magnetic probe measurements. The grid step size was chosen small enough to resolve the central current channel and the separatrices, yet large enough to allow the amount of data collected to be of manageable size and enable data collection to be accomplished in a finite time.

The poloidal magnetic field data is obtained by moving the probe to each position on the data grid, with the probe remaining in a poloidal plane, i.e., at a constant toroidal angle. The poloidal field is determined by measuring two orthogonal components in this plane. Since slight misalignment of the probe about its axis or out of the poloidal plane causes the toroidal field to be included in the poloidal field measurement, the probe signal from a pulse with the vacuum toroidal field only is used

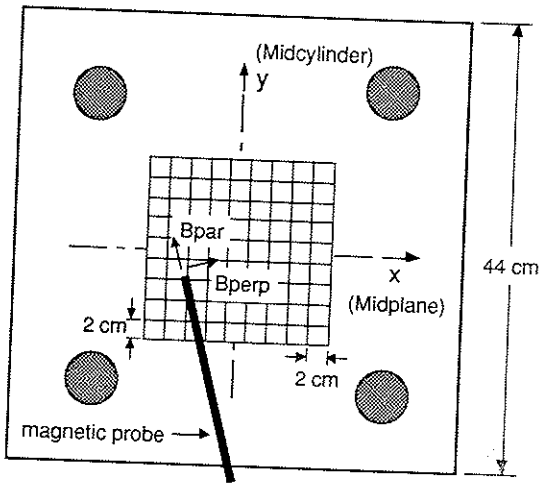

Figure 4.5
Tokapole II cross section showing the data grid and x-y coordinate system used in this research.

as a baseline. The magnitude of the poloidal magnetic field is given by:

$$B_{pol} = \sqrt{B_{par}^2 + B_{perp}^2} \qquad (4.1)$$

and the direction of the field with respect to the probe is given by:

$$\alpha = \tan^{-1} (B_{par} / B_{perp}) \qquad (4.2)$$

where the subscripts par and perp refer to the components of the magnetic field parallel and perpendicular to the probe axis, respectively. For ease of subsequent calculation, the data are transformed from probe coordinates to machine coordinates using Equation (4.2) and the angle that the probe makes with the machine wall. The poloidal field data are now expressed in B_x and B_y components. The origin of the x–y coordinate system is located at the machine center, and x is positive going radially out while y

is positive going up (see Figure 4.5). The sense of the voltage applied across the poloidal gap is known and thus the direction of the poloidal field can be determined. Therefore the raw poloidal field data can be plotted in vector form to check for gross discrepancies in the data. Equilibrium poloidal field vectors for a tokamak discharge with $q_a = 3$ are plotted in Figure 4.6. These data were obtained during the equilibrium or

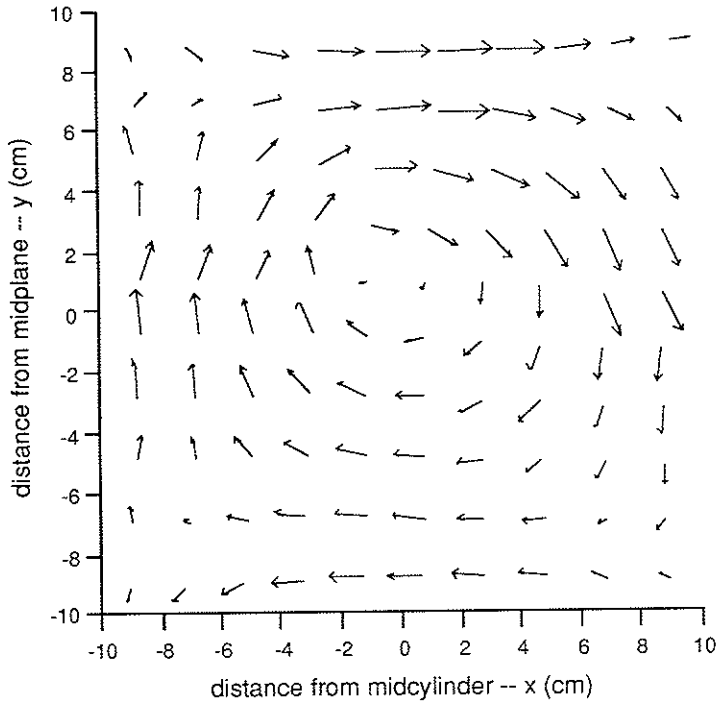

Figure 4.6
Equilibrium poloidal field vectors for a discharge with $q_a = 3$. These data were obtained 150 μsec before the first disruption, which is in the equilibrium portion of the discharge.

so called "flat-top" portion of the discharge, which is before the disruptions begin. The center of the discharge (the magnetic axis), the x-points, and the separatrix can be easily distinguished with this technique.

The toroidal magnetic field data were obtained with the same probes, although only the coil perpendicular to the probe axis was used. The coil is oriented to detect the magnetic field perpendicular to the plane in which the poloidal field was measured. Data were taken along the midplane for vacuum toroidal field pulses only. Plasma current modifications of the vacuum toroidal field have been found to be negligible (less than 5%) and thus will be ignored in further computations. Also, it has been found that the change in the toroidal field during disruptions is negligible and so a constant (in time) toroidal field profile will be used in further computations. The toroidal field profile can be fit very closely to $B_t \sim 1/R$, where R is the major radius of the machine (Figure 4.7).

The poloidal magnetic field data were analyzed, assuming toroidal symmetry, to produce plots of the poloidal magnetic flux function Ψ_p, profiles of the flux-surface-averaged safety factor $q(\Psi_p)$, and profiles of the toroidal current density J_t. The poloidal magnetic flux function is defined by:

$$\Psi_p(r,\theta) = \iint_{\theta=con} \vec{B} \cdot \overrightarrow{dS_p} = \iint_{\theta=con} \overrightarrow{B_p} \cdot \overrightarrow{dS_p} \qquad (4.3)$$

where (r,θ) are the cylindrical coordinates of a given point, $\vec{B}$ is the total magnetic field, $\overrightarrow{B_p}$ is the poloidal magnetic field, and $\overrightarrow{dS_p}$ is a differential

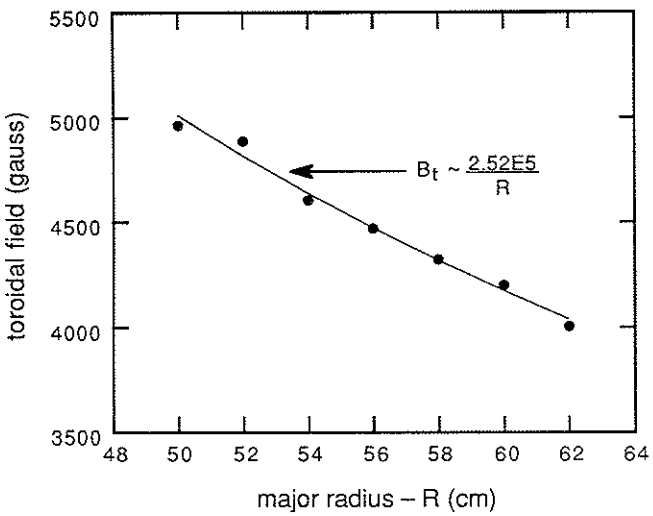

Figure 4.7
Vacuum toroidal field profile along the midplane

ribbon of area at a constant θ that extends from the magnetic axis to the point (r,θ) and is continuous in the toroidal direction. Substituting for $\overrightarrow{dS_p}$ in Equation (4.3) yields:

$$\Psi_p(r,\theta) = \int_0^r (2\pi R\, dr') \left|\vec{B} \times \hat{r}\right| = 2\pi \int_0^r dr' \, (R_0 + r'\cos\theta) \left|\vec{B} \times \hat{r}\right| \quad (4.4)$$

where R_0 is the major radius, $\hat{r}$ is a unit vector in the direction of integration, $\left|\vec{B} \times \hat{r}\right|$ is the component of the poloidal magnetic field perpendicular to $\hat{r}$, and r' is the radius. After rewriting to allow numerical calculation and using the coordinate system of Figure 4.5, Equation (4.4) becomes:

$$\Psi_p(r,\theta) = 2\pi \sum \Delta r' \, (R_0 + r'\cos\theta) \, (B_x \sin\theta - B_y \cos\theta) \quad (4.5)$$

where Δr' is the integration increment and the summation is carried out along a chord from the origin to the point r = (x,y). Since the data is only available at a small number of grid points, an interpolation must be performed to provide B_x and B_y data for all points in between the grid points. This is done by a two-dimensional interpolation software package. The routine is capable of extrapolation also, which is useful in constructing the outermost flux surfaces.

The integration (summation) begins at the magnetic axis of the discharge, which is determined by searching for the null in B_{pol}^2. The flux plots obtained from this method [Figure 4.8(a)] resemble those expected from numerical calculation [Figure 4.8(b)]. The separatrix and the x-points can be distinguished easily on the experimentally obtained flux plots. The flux plot of Figure 4.8(a) was determined at 150 μsec before the first disruption, which is during the equilibrium ("flat-top") portion of the discharge. The flux plot of Figure 4.8(b) is calculated by an equilibrium MHD code with typical Tokapole II parameters as inputs.

Once the magnetic surfaces have been obtained the flux-surface-averaged safety factor can be determined from Equation (2.4), which for one poloidal transit is:

$$q(\Psi_p) = \frac{\text{toroidal transits}}{\text{poloidal transits}} = \frac{\Delta\phi}{2\pi} \quad (4.6)$$

where φ is the toroidal angle. The definition of a magnetic field line can be expressed as:

$$\frac{dl_p}{B_p} = \frac{R\, d\phi}{B_t} \quad (4.7)$$

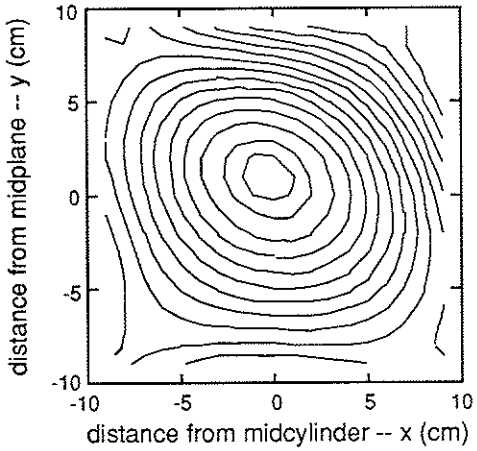

Figure 4.8(a)
Equilibrium poloidal flux contours determined experimentally during the "flat-top" of a discharge with $q_a = 3$.

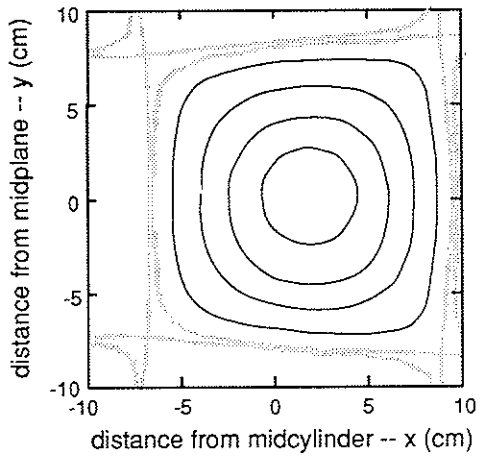

Figure 4.8(b)
Poloidal flux contours for a typical tokamak discharge calculated from an MHD equilibrium code. The separatrix is shown as the dotted lines.

where B_t is the toroidal field, B_p is the poloidal field (parallel to a flux surface and perpendicular to the toroidal field), R $d\phi$ is the toroidal path length, and dl_p is the poloidal path length (along a flux surface). Combining Equations (4.6) and (4.7) yields:

$$q(\Psi_p) = \frac{1}{2\pi} \oint \frac{B_t}{R\, B_p}\, dl_p \qquad (4.8a)$$

$$dl_p = \sqrt{dr^2 + r^2\, d\theta^2} \qquad (4.8b)$$

where r and θ are cylindrical coordinates and the integration is carried out along a closed flux surface. Rewriting Equations (4.8a) and (4.8b) to allow for numerical calculation yields:

$$q(\Psi_p) = \frac{1}{2\pi} \sum \frac{B_t}{R\, B_p} \sqrt{(\Delta r)^2 + r^2\, (\Delta\theta)^2} \qquad (4.9)$$

where $\Delta\theta$ is the angular separation of successive points along a particular flux surface and Δr is the difference in radius of these successive points.

An equilibrium safety factor profile for a discharge with $q_a = 3$ obtained by this method is plotted in Figure 4.9. This profile was calculated 150 μsec before the first disruption which is during the "flat-top" portion of the discharge. It is seen that the safety factor is less than one on axis and rises rapidly near the separatrix. The error bars shown on this plot are due to uncertainties in the magnetic field measurements and the location of the grid points along with the propagation of these measurement errors.

Assuming toroidal symmetry, the existence of circular flux surfaces, and using an infinite aspect ratio expansion, the local safety factor can be written as:

$$q = \frac{r\, B_t}{R_0\, B_p} \qquad (4.10).$$

A comparison of Equations (4.9) and (4.10) shows that these two-dimensional measurements are necessary since the non-circularity of Tokapole II discharges renders inferences of q from single chord measurements unreliable. That is, Δr becomes significant as the flux surfaces become progressively more non-circular as evidenced in Figures 4.8(a) and 4.8(b).

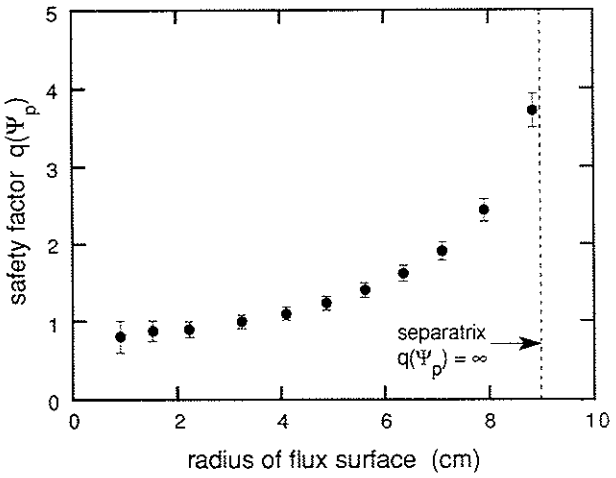

Figure 4.9
Equilibrium safety factor profile for a discharge with $q_a = 3$.

The toroidal current density profile can also be determined from the poloidal field measurements. The current density is defined by:

$$\vec{J} = \frac{1}{\mu_0} \nabla \times \vec{B} \qquad (4.11).$$

The component in the toroidal direction is the only one calculated, but the

data is complete enough to allow all components to be calculated. Rewriting the toroidal component of Equation (4.11) yields:

$$J_t = \frac{1}{\mu_0} \left(\frac{\partial B_y}{\partial x} - \frac{\partial B_x}{\partial y} \right) \qquad (4.12).$$

The derivative is performed using a second order central difference formula along with a second order forward/backward difference formula at the endpoints. Only data at the grid points is used for this derivative since an interpolation between data points would necessarily contribute its order to the result of the derivative.

Figure 4.10 shows an equilibrium toroidal current density profile determined 150 μsec before the disruptions begin in a discharge with q_a = 3. Data along a horizontal chord that extends through the magnetic axis of the discharge is plotted. The profile is peaked at a value of approximately 200 amps/cm^2 and the value of J_t at the edge of the central current channel agree with scrape-off current profiles obtained previously.[2] An integration of the two-dimensional toroidal current profile, as determined by this method, indicates that the total current flowing in the toroidal direction is consistent with the value obtained from the plasma current monitor. The error bars are determined from the uncertainties in the magnetic field measurements and the location of the grid points.

Since a single internal probe with one set of coils was used for these measurements, the data points were accumulated over many shots and positions within the plasma (at least three shots per position on the grid). The use of single probe with a single set of coils has some important limitations. First, the irregular nature of major disruptions gives rise to

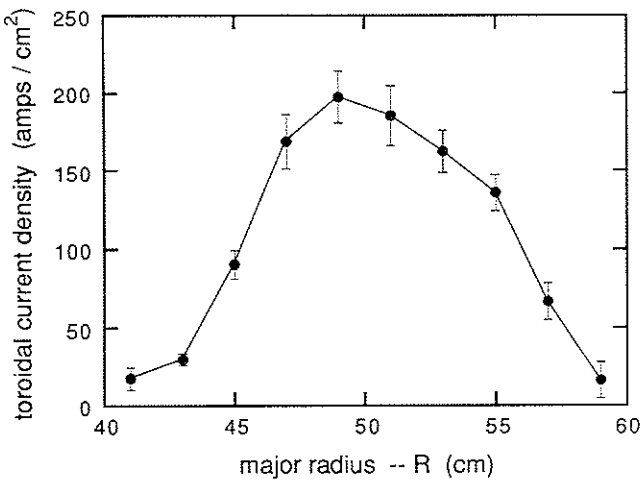

Figure 4.10
Equilibrium toroidal current density profile along a horizontal chord through the magnetic axis for a discharge with $q_a = 3$.

statistical uncertainties that limit the accuracy and time resolution possible in these shot-to-shot measurements. Secondly, the introduction of the probe to various points within the current channel causes a systematic perturbation of the plasma which is difficult to quantify and thus correct.

The first limitation is dealt with by searching the data-base for discharges with similar disruptions as measured by the central chord SXR detector. The criteria used are period and relative amplitude of the disruptions. This allows the magnetic field data from different discharges to be phase-referenced to the central chord SXR signal. Time resolution is

achieved by determining the poloidal magnetic field at a fixed time with respect to this phase-reference time for each discharge selected by the previously mentioned criteria.

The discharges remain unperturbed by the presence of the probe until the probe is within two or three centimeters of the magnetic axis. To deal with these small perturbations, the data-base is searched for discharges that have similar parameters such as total plasma current, edge poloidal field obtained from a monitor probe, and effective edge safety factor. This does not completely resolve the second limitation but it does keep the systematic errors introduced from the probe perturbation to a minimum.

REFERENCES

[1]T.H. Osborne, Ph.D. thesis, University of Wisconsin (1984).

[2]R.A. Moyer, Ph.D. thesis, University of Wisconsin (1988).

[3]R.J. Groebner, Ph.D. thesis, University of Wisconsin (1979).

[4]R.A. Moyer, R.N. Dexter, J.A. Goetz, S.C. Prager, and I.H. Tan, Bulletin of the American Physical Society, **31**, 1594 (1986).

[5]M.W. Phillips, University of Wisconsin Plasma Studies, PLP 765 (1978).

[6]N.S. Brickhouse, J.D. Callen, R.N. Dexter, D.E. Graessle, D. Kortbawi, R.A. Moyer, T.H. Osborne, S.C. Prager, J.S. Sarff, J.C. Sprott, E. Uchimoto, C.K. Chu, J. DeLucia, A. Deniz, R.A. Gross, A.A. Grossman, A. Holland, F.M. Levinton, M. Machida, T.C. Marshall, and G.A. Navratil, in *Plasma Physics and Controlled Nuclear Fusion Research 1984*, Proceedings of the 10th International Conference, London (IAEA, Vienna, 1985), Vol. 1, p. 385.

[7]M. Okabayashi, H. Maeda, H. Takahashi, and M. Reusch, Nuclear Fusion, **21**, 271 (1981).

[8]F. Karger, K. Lackner, G. Fussman, B. Cannici, W. Engelhardt, J. Gernhardt, E. Glock, D.E. Groening, O. Klüber, G. Lisitano, H.M. Mayer, D. Meisel, P. Morandi, S. Sesnic, F. Wagner, and H.P. Zehrfeld, in *Plasma Physics and Controlled Nuclear Fusion Research 1976* Proceedings of the 6th International Conference, Berchtesgaden (IAEA, Vienna, 1977), Vol. 1, p. 267.

[9]Equipe TFR, Nuclear Fusion, **17**, 1283 (1977).

[10]K. Toi, S. Itoh, K. Kadota, K. Kawahata, N. Noda, K. Sakurai, K. Sato, S. Tanahashi, and S. Yasue, Nuclear Fusion, **19**, 1643 (1979).

[11]K. McGuire and D.C. Robinson, Physical Review Letters, 44, 1666 (1980).

Chapter 5

Experimental Results and Discussion

The prime objective of this research has been to determine the behavior of the internal magnetic fields and thus the evolution of the central safety factor during major disruptions. To that end, total magnetic reconnection is observed during major disruptions in Tokapole II. Data that substantiates this claim will be presented in this chapter. These include poloidal magnetic fields, poloidal magnetic flux contours, flux-surface-averaged safety factor profiles, and toroidal current density profiles. The reasons for believing that total magnetic reconnection occurs will be discussed. Suggestions for future work on total magnetic reconnection will also be presented in this chapter.

V.A. Experimental Results for Plasmas with $q_a = 3$

The experimental method followed to obtain the internal magnetic fields, poloidal magnetic flux contours, and safety factor and toroidal current density profiles is discussed in Section IV.B. Figure 5.1 shows the measured magnetic fields in a poloidal plane along with the central chord SXR signal for a discharge with $q_a = 3$. Near the magnetic axis, the major disruptions appear as giant sawteeth on the magnetic pickup coils. The relative phasing of the magnetic fields with respect to the central chord

SXR signal is shown on the figure. The pre-disruption, post-disruption, and reheat phases of a major disruption in Tokapole II are also shown. The phase referencing is vitally important as it allows data collected from many different discharges to be used to compute a global plasma quantity.

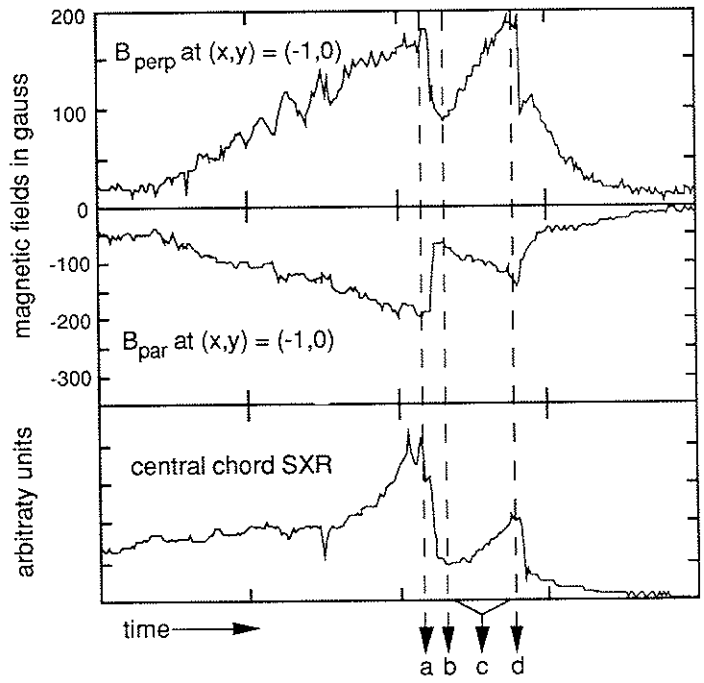

Figure 5.1
Temporal evolution of the magnetic fields measured with an internal probe and the central chord SXR signal in a discharge with $q_a = 3$. The relative phasing of the magnetic signals to the SXR signal is shown (a) before the first disruption, (b) after the first disruption, (c) during the reheat phase of the disruption, and (d) before the second disruption.

V.A.1. Poloidal Magnetic Field Measurements

The poloidal field vectors measured 25 μsec before the first disruption, 25 μsec after the first major disruption, and 25 μsec before the second disruption are plotted in Figures 5.2(a), 5.2(b), and 5.2(c) respectively. The magnetic axis, the x-points, and the separatrix can easily be distinguished on these plots. The magnetic axis is located where the

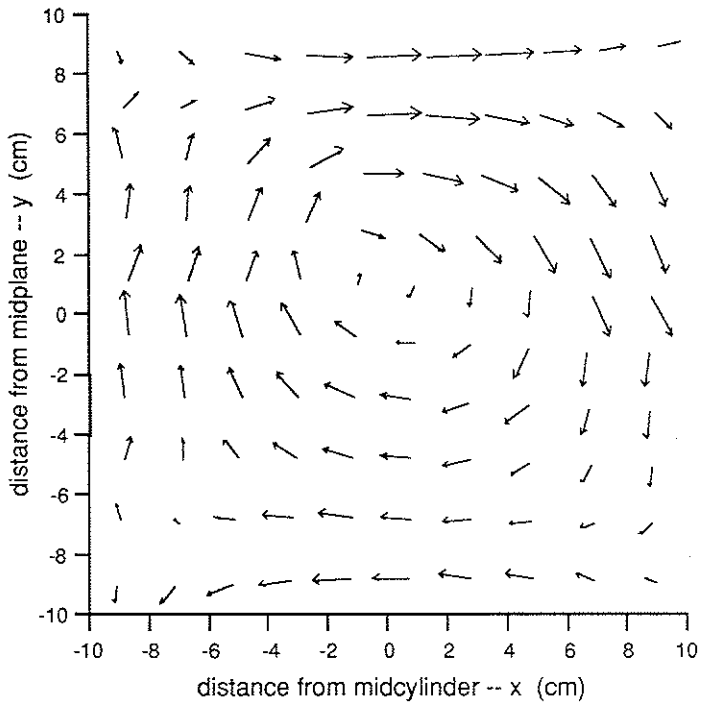

Figure 5.2(a)
Poloidal field vectors 25 μsec before the first major disruption in a discharge with $q_a = 3$.

poloidal field vanishes. The separatrix and its x-points are distinguished by the change in direction of the poloidal field.

It is seen that the magnetic axis moves inward during a major disruption and that the poloidal field near the center of the plasma column decreases dramatically after a major disruption. The magnetic axis moves inward during the first disruption, from (x, y) = (-0.1, +1.1) to

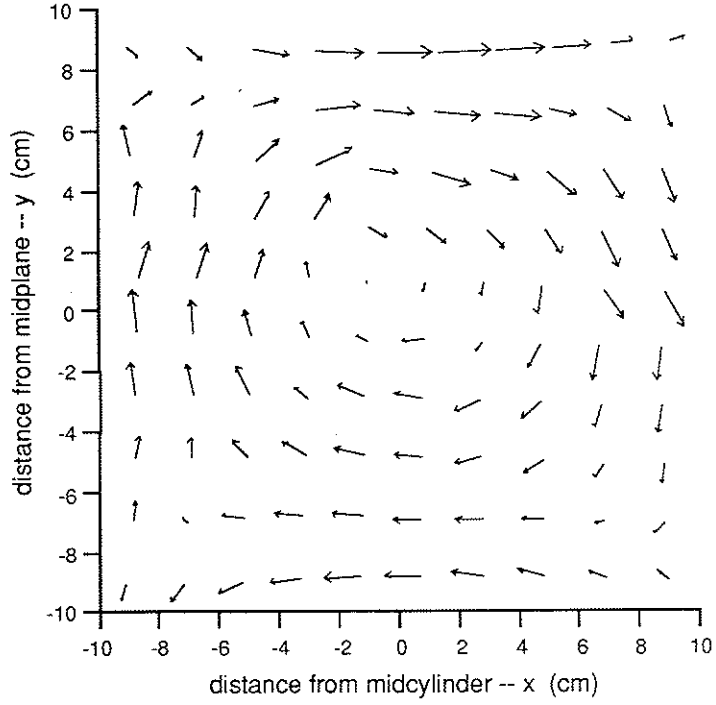

Figure 5.2(b)
Poloidal field vectors 25 μsec after the first major disruption in a discharge with $q_a = 3$.

(x,y) = (-1.0,+1.1), and then moves outward during the reheat phase until it is at (x,y) = (0.0,+1.2) before the second disruption. The poloidal field has a maximum magnitude of approximately 750 Gauss, with this value remaining relatively constant as the disruptions progress. This maximum value of the poloidal field occurs at the edge of the central current channel, that is, near the separatrix. The magnitude of the poloidal field

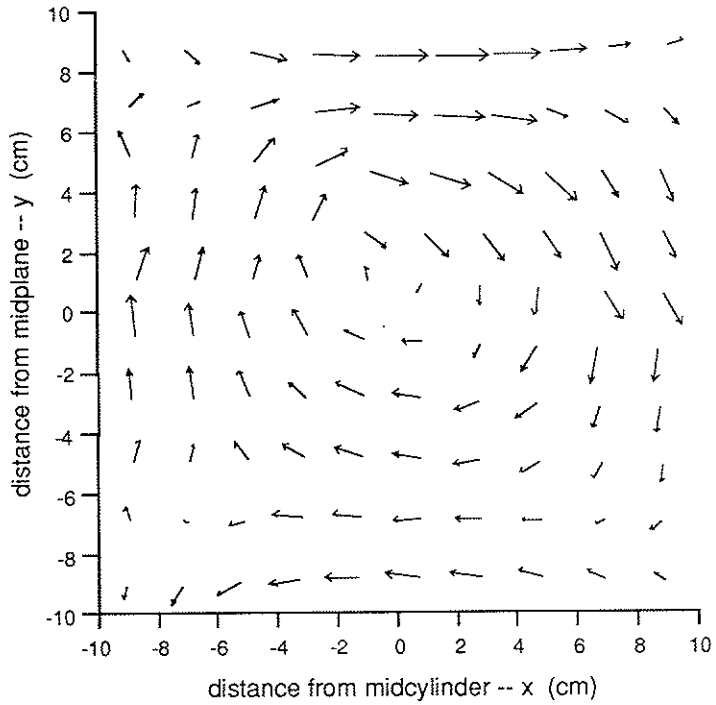

Figure 5.2(c)
Poloidal field vectors 25 μsec before the second disruption in a discharge with $q_a = 3$.

within five to six centimeters of the magnetic axis decreases dramatically (up to 50 percent) during a major disruption. The poloidal field increases during the reheat phase and reaches similar values before the second disruption as before the first disruption.

V.A.2. Poloidal Magnetic Surfaces

The poloidal flux contours measured 25 μsec before the first disruption, 25 μsec after the first major disruption, and 25 μsec before the second disruption are plotted in Figures 5.3(a), 5.3(b), and 5.3(c) respectively. The magnetic axis is marked with a cross on these figures, corresponding to the points previously listed. The separatrix and x-points

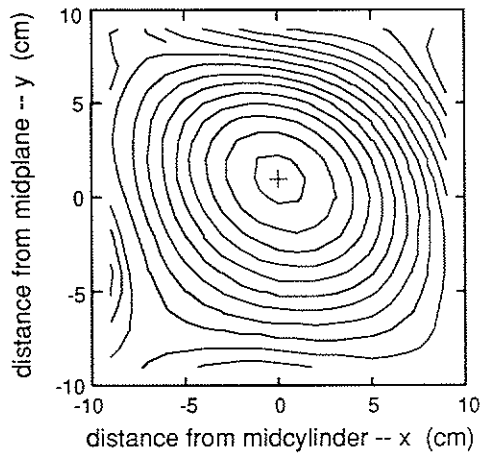

Figure 5.3(a)
Poloidal flux contours 25 μsec before the first disruption in a discharge with $q_a = 3$. The center of the discharge is marked with a cross.

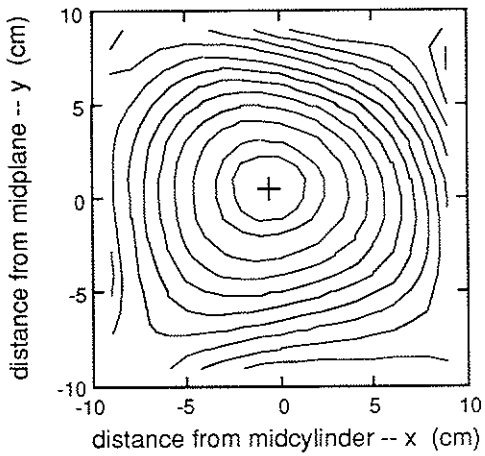

Figure 5.3(b)
Poloidal flux contours 25 μsec after the first disruption in a discharge with $q_a = 3$. The center of the discharge is marked with a cross.

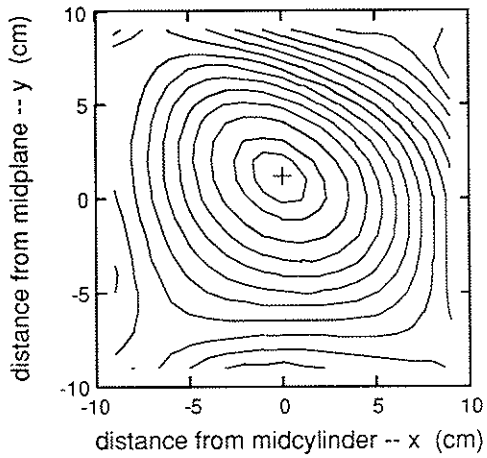

Figure 5.3(c)
Poloidal flux contours 25 μsec before the second disruption in a discharge with $q_a = 3$. The center of the discharge is marked with a cross.

can easily be distinguished on these experimentally obtained plots by locating the places at which the contour lines change curvature. These plots resemble those of Figures 3.3(b) and 4.8(b) which were generated numerically from an MHD equilibrium code. There are distortions in these experimental plots, most notably the upper, outer quadrant of Figure 5.3(c). These distortions could be indicative of a ring that is not in the correct place to create a symmetric equilibrium. Enhanced copper impurity emissions since the Tokapole II upgrade support this supposition.[1] The grid step size combined with the IDL routine used to plot the contours may also be the cause of the distortions. These distortions to the flux surfaces necessarily affect the calculation of the safety factor due to the aberration in the radius. However, since the distortions are always present, any change in the safety factor will be real. It is only the value of the safety factor that is affected by the distortions.

V.A.3. Flux-surface-averaged Safety Factor Profiles

The safety factor will be altered if total magnetic reconnection is occurring during major disruptions in Tokapole II. In particular, for total reconnection the center of the plasma column must be affected by the disruption. Figure 5.4 is a plot of the central flux-surface-averaged safety factor versus the radius of the flux surface on which the averaging was done. This abscissa is the average radius of the flux surface and is thus a marker for the ordinate points. The point at which the flux surface

intersects the outer midplane or flux coordinates with the separatrix defined as the plasma radius could also be used as the abscissa for Figure 5.4.

The profiles plotted in Figure 5.4 were measured 25 μsec before and 25 μsec after the first disruption in a series of discharges with $q_a = 3$. The value of q(0) before the disruption is 0.75 and rises to a value of 1.3 after a major disruption. The error bars shown in Figure 5.4 are due to uncertainties in the magnetic field measurements and the location of the

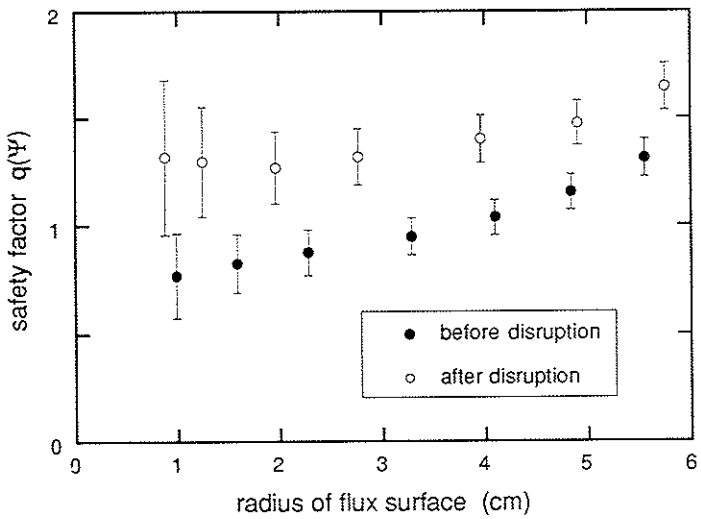

Figure 5.4
Flux-surface-averaged safety factor profile 25 μsec before (solid circles) and 25 μsec after (open circles) the first major disruption in a discharge with $q_a = 3$. Only the central points are shown to emphasize the change in the safety factor during a major disruption.

grid points, and the propagation of these measurement errors. The error bars become large near the center (as compared to the edge) due to the fact that both the poloidal field and the radius are tending to zero and thus the relative error in their determination increases. Thus, this change in the central safety factor during a major disruption is significant and indicates that total magnetic reconnection has occurred. This change, coupled with the fact that the total plasma current remains constant during a disruption, indicates that there has been a rearrangement of the current density profile. This rearrangement is also a signature of total reconnection.

The complete flux-surface-averaged safety factor profile 25 μsec before and 25 μsec after the first disruption in a discharge with $q_a = 3$ is shown in Figure 5.5. The separatrix, where q (Ψ) should tend to infinity, is shown as a dotted line on the figure. Both profiles do indeed tend to infinity as the separatrix radius is approached. The safety factor profile after the disruption is flat over the inner four to five centimeters. This radius corresponds approximately to the location of the q = 1.3 radius before the disruption. This flattening of the profile is also an indication that total reconnection has occurred. In the region from the q = 1.3 radius to the separatrix, the safety factor is slightly higher after the disruption. The difference between the safety factor profiles in this region is not as significant as the differences in the center. That is to say, the major disruption affects the center more than it affects the periphery.

During the reheat phase of a disruption the plasma is heated by the

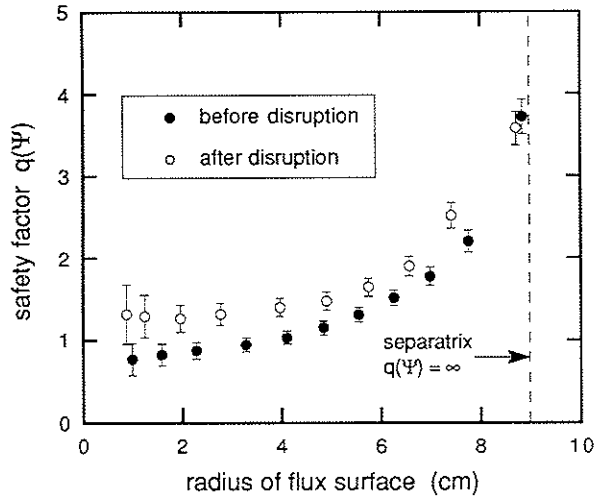

Figure 5.5
Flux-surface-averaged safety factor profile 25 μsec before (solid circles) and 25 μsec after (open circles) the first disruption in a discharge with $q_a = 3$. The location of the separatrix ($q(\Psi) = \infty$) is denoted with a dashed line.

Ohmic currents, as indicated by the rise in the central chord SXR signal. Flux-surface-averaged safety factor profiles measured during the reheat phase of a major disruption are plotted in Figure 5.6. These profiles were obtained between the first and second major disruptions in a series of discharges with $q_a = 3$. The time slices chosen are 75 μsec after the first disruption, 125 μsec before the second disruption, and 25 μsec before the second disruption. These times are all relative to a disruption period of approximately 300 μsec, with the caveat that these periods change slightly

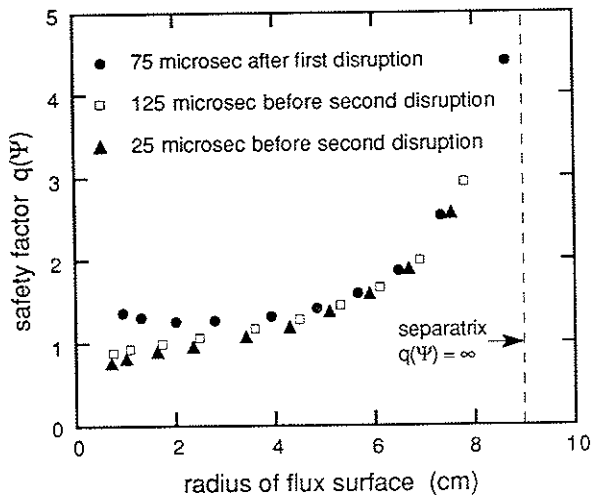

Figure 5.6
Flux-surface-averaged safety factor profiles during the reheat phase of a major disruption in a discharge with $q_a = 3$. The time slices shown are 75 μsec after the first (solid circles), 125 μsec before the second (open squares), and 25 μsec before the second (solid triangles) major disruption. The location of the separatrix ($q(\Psi) = \infty$) is denoted with a dashed line.

from discharge to discharge.

In accordance with the Kadomtsev model of reconnection[2], the safety factor on axis decreases from its post-disruption value to q(0) = 0.75 just before the second disruption. This central q value is identical (within error bars) of the value obtained before the first disruption. During this dramatic change in q(0), the region from five centimeters to the separatrix

is not changed significantly.

V.A.4. Toroidal Current Density Profiles

As mentioned previously, since the central safety factor changes from below one to above one during a major disruption while the total plasma current remains constant, the current density profile must be rearranged. The toroidal current density profile on a horizontal chord through the magnetic axis is plotted in Figure 5.7. The profiles shown were obtained 25 μsec before and 25 μsec after the first disruption in a series of discharges with $q_a = 3$. The current density profile before the first disruption is peaked near the magnetic axis at a value of approximately 200 amps/cm^2. After the first disruption, the profile is flattened over the inner eight to ten centimeters of the plasma column at a value of 120 – 140 amps/cm^2. This flattened region corresponds to the region in flux space over which the safety factor profile is also flattened by the disruption.

An integration of the two-dimensional toroidal current density profile indicates that the total current flowing in the toroidal direction does not change significantly during the major disruption, consistent with the independent measurement of the plasma current as discussed in Section III.B. Also, the value obtained is consistent with that obtained from other measurements of the total current.

Toroidal current density profiles measured during the reheat phase of a major disruption are plotted in Figure 5.8. These profiles were obtained between the first and second major disruptions in a series of

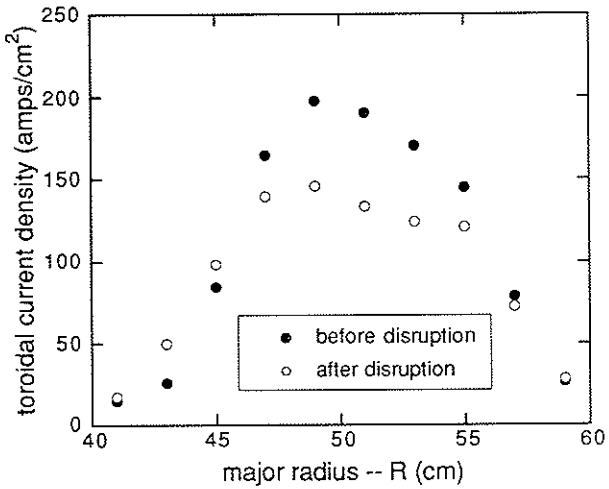

Figure 5.7
Toroidal current density profile 25 μsec before (solid circles) and 25 μsec after (open circles) a major disruption in a series of discharges with $q_a = 3$.

discharges with $q_a = 3$. The time slices chosen are 75 μsec after the first disruption, 125 μsec before the second disruption, and 25 μsec before the second disruption. During the reheat the current density profile becomes peaked, reaching a value of approximately 190 amps/cm^2 on axis before the second disruption. The profile over the outer five centimeters on the outboard side does not change significantly during the reheat while the current density on the inboard side decreases until its shape is similar to that before the first disruption. Throughout the reheat phase of the

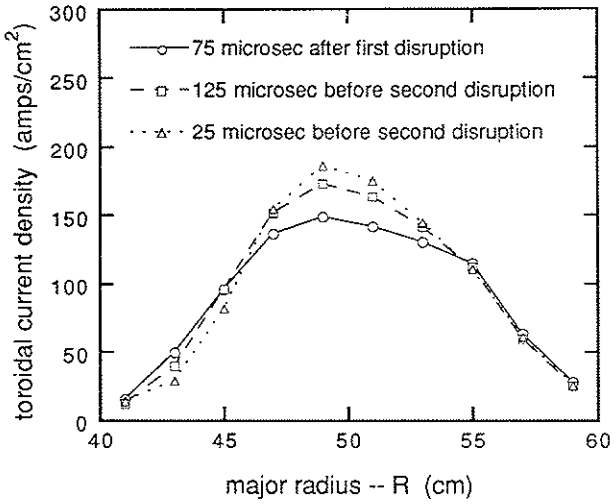

Figure 5.8
Toroidal current density profiles during the reheat phase of a major disruption in a discharge with $q_a = 3$.

disruption, the total current flowing in the toroidal direction does not change as indicated by an integration of the two-dimensional current density profile.

V.B. Summary of Experiments

The experiments described in this thesis were performed in order to determine whether or not total magnetic reconnection is occurring during

major disruptions in Tokapole II. To that end, the behavior of the central safety factor has been investigated by measuring the internal magnetic fields, calculating the poloidal magnetic flux function, and then determining the flux-surface-averaged safety factor profile. Also, the internal magnetic field measurements allow the toroidal current density to be calculated. All these measurements and calculations are time resolved, which allows them to be tracked through all phases of a major disruption. This investigation is unique in that it is a fully two-dimensional, direct measurement of the internal magnetic fields. Also, the lack of impurity influx owing to the absence of limiter contact allows the plasma to survive a major disruption.

It is observed that q(0) rises from 0.75 to 1.3 during a major disruption. The plasma current is redistributed during a major disruption, with the current density profile going from a peaked profile to a flat profile (over the inner eight to ten centimeters of the plasma column). During the reheat phase of a major disruption, q(0) decreases until it reaches a value similar to that prior to the previous disruption. Also, the current density profile again becomes peaked during the reheat. These observations, coupled with the fact that the total plasma current remains unchanged, are strong evidence that complete reconnection occurs during major disruptions in Tokapole II. However, the details of the reconnection process are less clear.

Major disruptions in Tokapole II have m/n = even/odd precursor oscillations on SXR detectors and magnetic coils placed outside the separatrix show a growing precursor oscillation of even m and odd n. The

magnetic oscillations are not purely sinusoidal but are distorted in a manner consistent with an m/n = 3/2 mode and a m/n = 2/1 mode rotating together with the same toroidal angular velocity in the electron diamagnetic drift direction.[3] Apparently, the reconnection is not simply the growth of a single magnetic island resonant with the q = 3/2 or the q = 2/1 surface.

This observation of magnetic reconnection is in contrast to previous measurements of a stationary central q (absence of total reconnection) during sawtooth oscillations in the same device[4]. This indicates that the reconnection process is not identical for sawtooth oscillations and major disruptions in Tokapole II.

Safety factor measurement during sawtooth oscillations and disruptions in other tokamaks also yield contradictions. Some tokamaks[5,6,7] report that measurements of q(0) do not indicate total reconnection. In yet other tokamak experiments,[8,9,10] q(0) is roughly unity during a sawtooth cycle with insufficient resolution to discern the time variation in q(0) and the occurrence of total reconnection. It appears from all of these observations that the underlying physical cause of sawtooth oscillations and major disruptions may not be unique, that is, there may not be a single explanation for disruptive instabilities in the tokamak configuration.

V.C. Suggestions for Future Work

Tokapole II can be operated over a wide range of effective edge

safety factor, specifically $0.5 \leq q_a \leq 4$. This range of operating parameters gives rise to a variety of plasma instabilities which manifest themselves as sawteeth or disruptions on soft x-ray detectors. A summary of disruptive behavior in Tokapole II[11,12] is shown in Figure 5.9. It has been shown that for discharges in Tokapole II with $q_a < 1$ that the central safety factor remains stationary during sawtooth oscillations and that for discharges with $q_a = 3$, the central safety factor changes dramatically during major disruptions. In both instances the safety factor near the separatrix does not change significantly during a sawtooth or a major disruption.

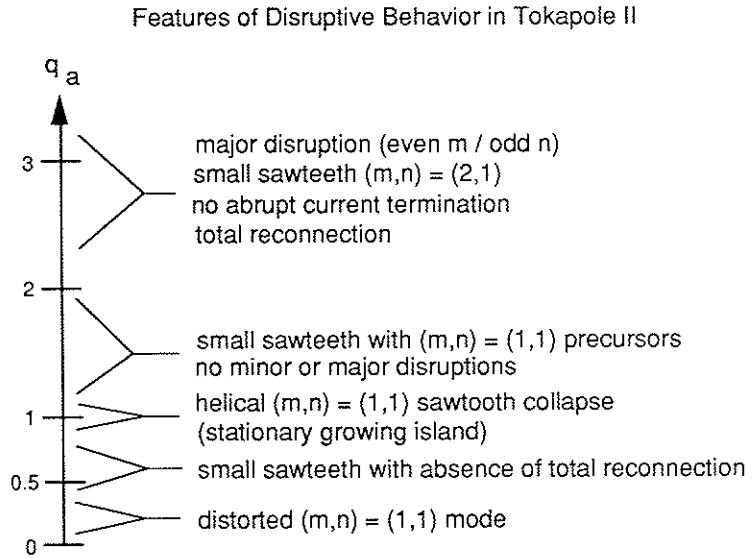

Figure 5.9
Key features of disruptive behavior in Tokapole II discharges over the range of operating parameters (revised from References 11 and 12).

At the extremes of the range of operating parameters for Tokapole II only the center of the discharge is affected (or not affected) by sawteeth or disruptions. This fact leads to the notion that "mini-flux plots" can be constructed in order to determine the behavior of the safety factor during instabilities in Tokapole II. A "mini-flux plot" would only cover the inner four or five centimeters of the plasma column. This would lessen the amount of data needed to construct a flux plot or else the flux plot could be of finer detail.

These flux plots could be constructed for discharges over the complete operating range of Tokapole II. Thus the behavior of the central safety factor would be determined for a variety of disruptive instabilities. The differences between discharges that do and do not exhibit total reconnection could be discerned, as well as whether a q_a threshold for total reconnection exists for disruptive behavior in Tokapole II.

The possibility also exists for measuring the safety factor profile during both sawteeth and disruptions for the same discharge. Prior to the upgrade to Tokapole II, high q_a discharges exhibited distinct small sawteeth along with major disruptions. Post-upgrade high q_a discharges also exhibit small sawteeth, but the sawteeth are not consistent enough for a shot-to-shot measurement to be performed. Also, when magnetic probes are inserted near the magnetic axis, the small sawteeth do not occur. However, in discharges with a 80:1 turns ratio in the poloidal field circuit, disruptions and sawteeth occur in the same discharge and the small sawteeth survive probe insertion.[13] These discharges allow for the possibility of investigating sawteeth and disruptions in the same

discharge.

The plasma physics group at the University of Wisconsin has acquired a large body of knowledge and experimental techniques for measuring safety factor profiles and magnetic fluctuations in the Tokapole II. Measurements of the fluctuation levels throughout the plasma column should be performed to determine the extent of turbulence during a sawtooth or a disruption. The upgrade of Tokapole II has the capability of performing Mirnov measurements to determine the influence of long wavelength MHD modes such as the (1,1), (2,1) and (3,2) modes. A complete picture of disruptive instabilities could be developed by simultaneously combining the safety factor profiles, the fluctuation level profiles, and the Mirnov measurements during each phase of a sawtooth or a disruption.

REFERENCES

[1]J.A. Goetz, R.N. Dexter, R.A. Moyer, S.C. Prager, J.C. Sprott, and I.H. Tan, Bulletin of the American Physical Society, **32**, 1903 (1987).

[2]B.B. Kadomtsev, Soviet Journal of Plasma Physics, **1**, 389 (1975).

[3]N.S. Brickhouse, J.D. Callen, R.N. Dexter, D.E. Graessle, D. Kortbawi, R.A. Moyer, T.H. Osborne, S.C. Prager, J.S. Sarff, J.C. Sprott, E. Uchimoto, C.K. Chu, J. DeLucia, A. Deniz, R.A. Gross, A.A. Grossman, A. Holland, F.M. Levington, M. Machida, T.C. Marshall, and G.A. Navratil, in *Plasma Physics and Controlled Nuclear Fusion Research 1984*, Proceedings of the 10th International Conference, London, (IAEA, Vienna, 1985), Vol. 1, p. 385.

[4]T.H. Osborne, R.N. Dexter, and S.C. Prager, Physical Review Letters, **49**, 734 (1982).

[5]H. Soltwisch, W. Stodiek, J. Manickam, and J. Schlüter, in *Plasma Physics and Controlled Nuclear Fusion Research 1986*, Proceedings of the 11th International Conference, Kyoto, (IAEA, Vienna, 1987), Vol. 1, p. 263.

[6]W.P. West, D.M. Thomas, J.S. DeGrassie, and S.B. Zheng, Physical Review Letters **58**, 2758 (1987).

[7]The JET Team, in *Plasma Physics and Controlled Nuclear Fusion Research 1988*, Proceedings of the 12th International Conference, Nice, (IAEA, Vienna, 1989), Vol. 1, p. 377.

[8]H. Weisen, G. Borg, B. Joye, A.J. Knight, and J.B. Lister, Physical Review Letters **62**, 434 (1989).

[9]D. Wróblewski, L.K. Huang, H.W. Moos, and P.E. Phillips, Physical Review Letters **61**, 1724 (1988).

[10]K. McCormick, F.X. Söldner, D. Eckhartt, F. Leuterer, H. Murmann, H. Derfler, A. Eberhagen, O. Gehre, J. Gernhardt, G.v. Gierke, O. Gruber, M. Keilhacker, O. Klüber, K. Lackner, D. Meisel, V. Mertens, H. Röhr, K.-H. Schmitter, K.-H. Steuer, and F. Wagner, Physical Review Letters **58**, 491 (1987).

[11]T.H. Osborne, Ph.D. thesis, University of Wisconsin (1984).

[12]R.A. Moyer, Ph.D. thesis, University of Wisconsin (1988).

[13]M.A. LaPointe, Ph.D. thesis, University of Wisconsin (1990), (private communication).